Università degli Studi di Napoli "Federico II"

Radio constraints on dark matter annihilation in the galactic halo and its substructures

PhD Thesis

Author:E. Borriello

Tutor: Prof. G. Miele

November 28, 2008

Contents

Ringraziamenti

Il mio primo ringraziamento va a Rino, per tutti i consigli, la disponibilità, l'aiuto e l'amicizia dimostrati in questi anni.

Vorrei inoltre ringraziare tutti i colleghi del gruppo Astroparticellare di Napoli, ma in particolare Ofelia ed Alessandro, con cui ho avuto il piacere di lavorare di più.

Sono estremamente grato a Sergio, Urbano e a tutti i colleghi di Valencia per la loro straordinaria ospitalità. L'anno trascorso con loro lo ricorderò a lungo.

Grazie a tutti coloro il cui aiuto non trova immediato riscontro in queste pagine, ma che è sempre stato ugualmente, o più, importante. Grazie di cuore a Viviana, Vincenzo, Javi e Teresa.

Grazie, infine, ai miei genitori.

Introduction

Cosmology and Astrophysics provide nowadays a compelling evidence of the existence of Dark Matter (DM) [1, 2]. Nevertheless, its nature still remains elusive, and Dark Matter constituents have escaped a direct detection in laboratory so far. Promising candidates are DM particles produced in thermal equilibrium in the early universe, the so-called Weakly Interacting Massive Particles (WIMPs). Theoretically models of WIMPs naturally arise, for example, in SUSY as the Lightest Super-symmetric Particle or as the Lightest Kaluka-Klein Particle in the framework of extra-dimensions. These candidates are self-conjugate and can thus annihilate in couple to produce as final states: neutrinos, photons, electrons, light nuclei (as wells as their antiparticles), etc., which can in principle be detected.

Among the indirect DM detection channels, gamma-ray emission certainly represents one of the most promising opportunity due to the very low attenuation in the interstellar medium, and to its high detection efficiency [2, 3, 4]. The neutrino detection rates expected in the current and forthcoming detectors are instead quite low [5, 6]. Finally, positrons and protons once produced by DM annihilation, strongly interact with gas, radiation and magnetic field in the galaxy thus the expected signal sensibly depends on the assumed propagation model [7, 8, 9]. However, during the process of thermalization in the galactic medium the high energy e^+ and e^- release secondary low energy radiation, in particular in the radio and X-ray band, that, hence, can represent a chance to look for DM annihilation. Furthermore, while the astrophysical uncertainties affecting this signal are similar to the case of direct e^+, e^- detection, the sensitivities are quite different, and, in particular, the radio band allows for a the discrimination of tiny signals even in a background many order of magnitudes more intense.

Indirect detection of DM annihilation through secondary photons has received recently an increasing attention, exploring the expected signature in X-rays [10, 11, 12], at radio wavelengths [13, 14, 15, 16] , or both [17, 18, 19]. In this thesis I will focus my analysis on the radio signal expected from the Milky Way halo and its substructures. It is worth noticing that the halo

signal has been recently discussed in Ref.s [20, 21, 22] in connection to the WMAP Haze, which has been interpreted as a signal from DM annihilation. In this concern I will take a more conservative approach, by assuming that the current radio observations are entirely astrophysical in origin, and thus deriving constraints on the possible DM signal. The main point will be the use of further radio observations besides the WMAP ones, in the wide frequency range 100 MHz-100 HZ, and a comparison of the achievable bounds. Furthermore, the model dependence of these constraints on the assumed astrophysical inputs will be analyzed. I will also discuss the detection perspectives of the signal coming from the brightest DM substructures in the forthcoming radio surveys.

The thesis is organized as follow: in chapter 1 I will discuss the astrophysical inputs required to derive the DM signal as the structure of the magnetic field, the DM spatial distribution and the interstellar radiation field. Chapter 2 is a brief review on cosmological and particle physics concept. In chapter 3 I describe in detail the processes producing the DM radio signal either when it is originated from the halo or from the substructures. In chapter 4 I present the currently available radio data and use them to derive constraints on DM.

Chapter 1

Astrophysical and cosmological inputs

1.1 The missing mass problem

The discovery made by Fritz Zwicky in 1933 [23] that visible matter accounts for only a tiny fraction of the total mass in the universe turned out to have been one of the most profound new insights produced by astronomical exploration during the past century.

From observations of the radial velocities of eight galaxies in the Coma Cluster, Zwicky found an unexpectedly large velocity dispersion, 1019 ± 360 km s^{-1}. Zwicky concluded from these observations that, for a velocity dispersion of 1000 km s^{-1}, the mean density of the Coma Cluster would have been 400 times greater than what is derived from luminous matter. He overestimated the mass-to-light ratio of the Coma Cluster because he assumed a Hubble parameter $H_0 = 588$ km s^{-1} Mpc^{-1} instead of the value we now know it posses, $H_0 = 72.4$ km s^{-1} Mpc^{-1} [1]. At that time, in fact, the Hubble's prestige was so great that none of the early astonomers thought of reducing Hubble's constant value to lover the mass-to-light ratios they founded. His value for the overdensity of the Coma Cluster should therefore be reduced from 400 to $(72.4/588) \times 400 \sim 50$.

Zwicky wrote: "If this [overdensity] is confirmed we would arrive at the astonishing conclusion that dark matter is present [in Coma] with a much greater density than luminous matter." This was the very first time the *dark matter* (in it's modern sense) made its appearance into scientific literature.

Zwicky continued: "From these considerations it follows that the large velocity dispersion in Coma (and in other clusters of galaxies) represents an unsolved problem." It is not yet clear what the basis was for Zwicky's claim

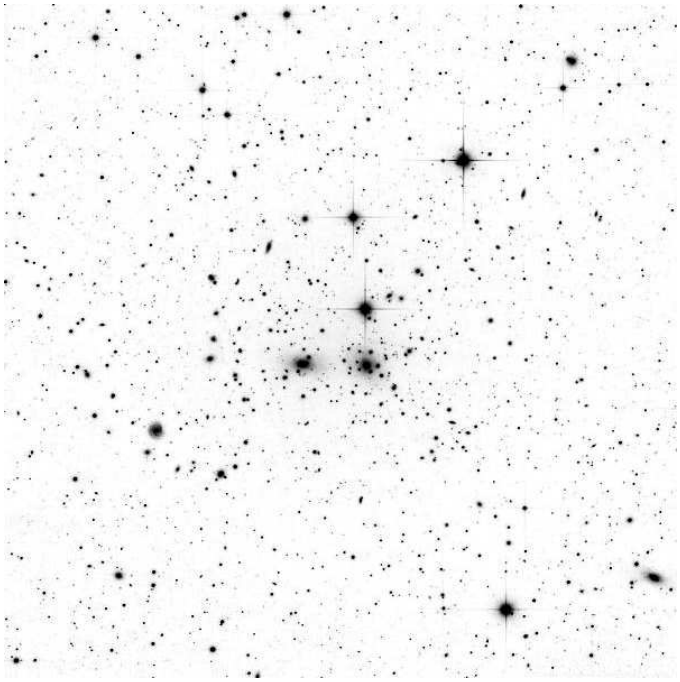

Figure 1.1: Coma cluster in negative B&W.

that other clusters also exhibited a missing mass problem. Not until 3 years later (1936) Smith found that the Virgo Cluster also appears to exhibit an unexpectedly high mass [24].

In 1959 Kahn and Woltjer pointed out that M31 and the Milky Way were moving toward each other, so that they must have completed most of a (very elongated) orbit around each other during a Hubble time [25]. Under this assumption that M31 and the Galaxy started to move apart 15 Gyr ago, they found that the mass of the Local Group had to be $\gtrsim 1.8 \times 10^{12} M_{\odot}$. Assuming that the combined mass of the Andromeda galaxy and the Milky Way system was $0.5 \times 10^{12} M_{\odot}$ Kahn and Woltjer concluded that most of the mass of the Local Group existed in some invisible form.

1.2 Rotation curves of spiral galaxies

So, dark matter manifested itself for the first time in clusters of galaxies, but it is on smaller scales that it gave the clearest and till now most robust, evidence of its existence. It clearly shows its presence is galaxies like our own, but astronomers had to wait nearly forty years to become aware of this.

Observations of the 21–cm radio emission from rotating clouds of neutral

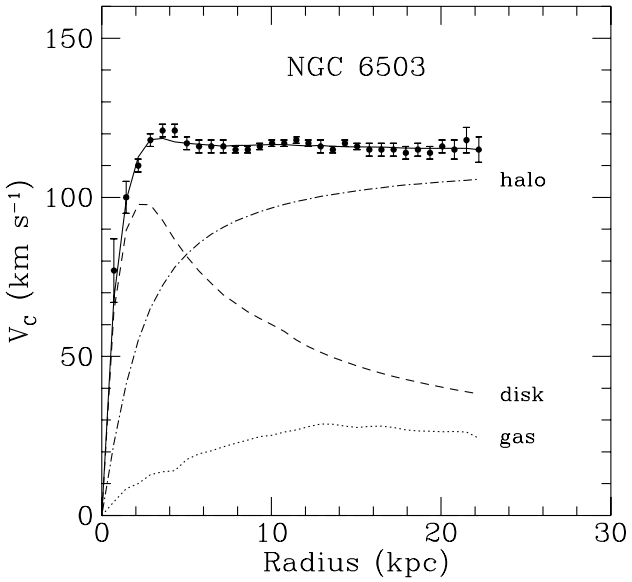

Figure 1.2: Rotation curve for the spiral galaxy NGC6503 [27].

hydrogen bounded to our galaxy determined the detailed rotation curve of the Milky Way as well as other spiral galaxies to be flat much beyond their extent as seen in the optical band.

Assuming a balance between the gravitational and centrifugal forces within Newtonian mechanics, the orbital speed V_C is expected to fall with the galactocentric distance r as $V_C^2 = GM/r$ beyond the physical extent of the galaxy of mass M. The run of V_C against r, for distances less than the physical extent, then leads to the distribution $M(r)$ of mass within radius r. The observation $V_C \approx$ constant for large enough r, to the largest r, up to ten times the radius of the luminous disk, thus showed that there is substantial amount of non luminous matter beyond even this largest distance [26].

The simplest way to justify a linearly increasing mass $M(r) \propto r$ is to assume that dark matter is present in a approximately spherical, isothermal, halo surrounding the disk, $\rho(r) \propto 1/r^2$.

Fig. 1.2 shows one of such rotation curves. Rotation velocities measurements are shown as a function of distance from the galactic center. The dashed and dotted curves are the contributions to V_C due to the disc and the gas, respectively, while the dot-dash curve represents the contribution from the dark halo.

1.3 Cosmological abundance of dark matter

As we saw, the first environments in which the dark matter presence was initially deduced was astrophysical, but it was from an analysis of the WMAP [1] data that we finally knew the DM total amount in the universe.

Let us first review the main equations that general relativity predicts for an homogeneous and isotropic universe and then define the so called "cosmological abundance, Ω_X, of a generic constituent X of the universe.

In general relativity, Einstein's equations relate the geometry of the universe locally to the energy momentum content. The geometry is expressed via the metric g_{ab} and subsequently through the Ricci Tensor R_{ab} and the curvature scalar R, while the energy momentum tensor is commonly denoted by T_{ab}. Using the reduced Planck mass $M_P = (8\pi G)^{-1/2}$, *Einstein's equation* read

$$T_{ab} = M_P^2 \left(R_{ab} - \frac{1}{2} g_{ab} R \right) \tag{1.1}$$

The cosmological constant, Λ, is already assumed to be part of the energy momentum tensor.

In order to solve these very complicated, coupled differential equations analytically, one needs to guess the geometry of the space and hence the metric. The most general metric that is isotropic and homogenous on constant time hyper-surfaces is the *Friedman-Lemaitre-Robertson-Walker metric*:

$$ds^2 = -dt^2 + a^2(t) \left(\frac{dr^2}{1 - kr^2} + r^2 d\theta + r^2 \sin^2 \theta d\phi^2 \right) \ . \tag{1.2}$$

Here $k = -1, 0, +1$ corresponds to open, flat and closed geometries.

For flat geometries (the case we will concentrate on), this can be written in terms of the cartesian coordinates x^i as

$$ds^2 = -dt^2 + a^2(t) \delta_{ij} dx^i dx^j \ . \tag{1.3}$$

The only possibility for the energy momentum tensor T_{ab} compatible with the assumptions of homogeneity and isotropy of the universe is:

$$T_{ab} = (\rho + p) u_a u_b + p g_{ab} \ , \tag{1.4}$$

that is the energy momentum tensor describing a *perfect fluid* with energy density ρ and pressure p. The relation between ρ and p is expressed in the equation of state $p = w\rho$ For non-relativistic matter, the pressure vanishes ($w = 0$), whereas photons and massless neutrinos have $w = 1/3$.

From the $0-0$ and $i-i$ part of Einstein's Equation (1.1), we get the *Friedmann equation*

$$3M_P^2\left(H^2+\frac{k}{a^2}\right)=\rho\ , \tag{1.5}$$

having defined the *Hubble parameter* H as

$$H=a^{-1}\frac{da}{dt}\ , \tag{1.6}$$

The ratio of the energy of some species ρ with the so-called critical energy density $\rho_{cr}=3M_P^2H^2$ is defined as

$$\Omega=\frac{\rho}{\rho_{cr}}\ . \tag{1.7}$$

For a flat universe (as suggested by the inflationary paradigm, by WMAP measurements and the fact that if curvature is small today it was practically zero immediately after the Big Bang), Ω is just the fraction a given species contributes to the total energy of the Universe. This is what is commonly called "cosmological abundance" of that species.

After five years of observations the estimates WMAP gives for the total amount of matter, Ω_m, and the amount of baryonic matter only, Ω_b, are

$$\Omega_m=0.258\pm0.030 \qquad \Omega_b=0.0462\pm0.0015\ . \tag{1.8}$$

The large discrepancy between this two values states that ordinary matter only constitutes a 2% of the total matter of the Universe. In the following chapter we will return on this point and we will see how the attempts to give a solution to the consistency problems of the Standard Model of elementary particles suggests quite naturally a possible explanation for the existence of this great amount of non-baryonic dark matter.

1.4 Dark matter distribution

It is quite obvious that the understanding of how DM is distributed around us is of fundamental importance for the calculation of every type of DM signal we can expect from our Galaxy. Unfortunately indirect observations (e.g. from rotation curves) are insufficient to constraint the shape of the density profile of the Milky Way. So our knowledge relay basically on N-body simulations.

Since the first simulation of the evolution of a galaxy cluster, in 1941 [28], our computational capabilities have saw an incredible growth. It was

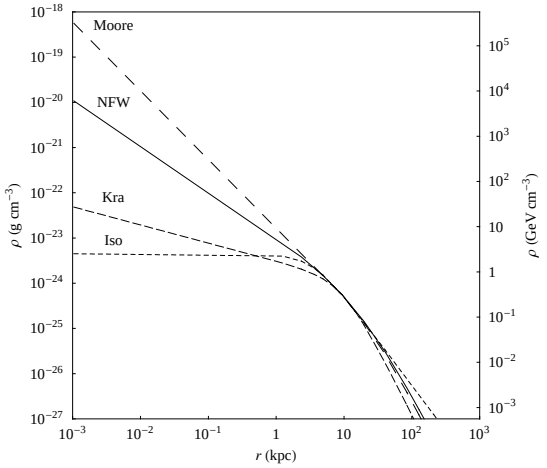

Figure 1.3: Some of the DM density profiles usually considered in literature.

using such a simulation that Navarro, Frank, and White (NFW) first shown, in 1996, that DM seems to aggregate following a sort of universal density profile [29],

$$\rho(r) = \rho_0 \left(\frac{r}{r_0}\right)^{-1} \left(1 + \frac{r}{r_0}\right)^{-2} , \tag{1.9}$$

parameterized by a length parameter r_0 and a density mass parameter ρ_0.

After this first result many other simulation were made, confirming or not the NFW profile. In particular there is a lot of uncertainty on the value of power-law index describing the mass profile of the innermost part of the galaxy. The majority of these different results can be resumed in a compact way in the form of a parameterized density profile:

$$\rho(r) = \rho_0 \left(\frac{r}{r_0}\right)^{-\gamma} \left[1 + \left(\frac{r}{r_0}\right)^{\alpha}\right]^{(\gamma-\beta)/\alpha} . \tag{1.10}$$

It reproduces the NFW profile for $\alpha = 1$, $\beta = 3$, and $\gamma = 1$. Other models, often encountered in literature are resumed in table 1.1. For more recent analysis see [30, 31, 32, 33].

In the following we will use a NFW profile to describe the dark matter halo distribution. Note, anyway, that this choice is quite conservative with respect to i.e. other proposed profiles like the Moore profile [34], which exhibits an internal cusp $\propto r^{-1.5}$ that would give in principle a divergent DM annihilation signal. A problem related to the NFW profile is that the mass enclosed is

	α	β	γ	r_0	Ref.
kra	2	3	0.4	10	[38]
NFW	1	3	1	20	[29]
Moore	1.5	3	1.5	28	[34]
Iso	2	2	0	3.5	[39]

Table 1.1: Coefficient of the density profile definided by eq. (1.10)

logarithmically divergent thus a regularization procedure is required to define the halo mass. Following the usual conventions we define the mass of the halo as the mass contained within the *virial radius* $r_{\rm vir}$, defined as the radius within which the mean density of the halo is $\delta_{\rm vir} = 200$ times the mean *critical cosmological density* ρ_{cr} which, for a standard cosmological model ($\Omega_m \simeq 0.3, \Omega_\Lambda \simeq 0.7$ [1]) is equal to $\rho_{cr} \simeq 5 \times 10^{-6}\text{GeV/cm}^3$.

The parameters describing the halo are determined imposing the local value of the DM density, ρ_S, and the Milky Way virial mass. The next paragraph is devoted to the first of these two observables. Moreover, to assign the virial mass of the DM halo we have first to take into account the inhomogeneities in the dark matter distribution predicted by numerical simulations.

1.4.1 Local dark matter density

Despite technical difficulties, the determination of the local value of the dark matter density ρ_S is, in principle, a simple task. It requires a very accurate knowledge of the rotation curve shape (this is the technical difficulty, especially if we are talking about our Galaxy) and a good understanding of how matter is distributed among the disk, the bulge, and the halo.

Let's calculate at least the order of magnitude of ρ_S. We will working in the simplest hypothesis. We know that the mass contained in a sphere of radius r has to fulfill the equation $dM/dr = v^2/G = \text{constant}$ (at large r) to reproduce the result $v^2 = GM(r)/r = \text{constant}$, so we assume that

$$M(r) = 4\pi \int_0^r r'^2 \rho(r') dr' \qquad \text{with} \qquad 4\pi r^2 \rho(r) = \frac{v^2}{G} \ .$$

So

$$\rho(r) = \frac{v^2}{4\pi G r^2} = \frac{v^2}{4\pi G R_S^2} \left(\frac{r}{R_S}\right)^{-2} \ .$$

At the Solar System distance, $R_S = 8.5$ kpc, we obtain

$$\rho_S = \frac{v^2}{4\pi G R_S^2} \ .$$

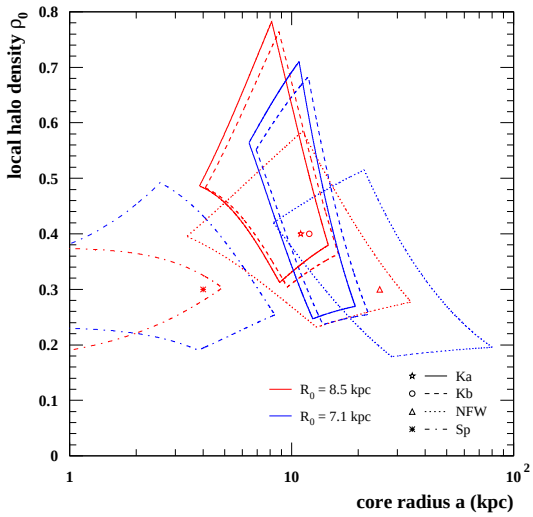

Figure 1.4: The range of local dark matter densities acceptable with observations of rotation curves for a variety of halo profiles and galactocentric distances. From Ref. [39].

Using an asymptotical velocity $v \sim 100$ km s^{-1} we deduce

$$\rho_S \sim 0.1$$

GeVc^{-2}cm^{-3} .

The very sophisticated analysis performed by various group show very different values for ρ_S, but its order of magnitude is in accord with this simple estimate. Fig. 1.4 show the acceptable range of local dark matter densities, $0.2 - 0.8\,\mathrm{GeV/cm^3}$, coming out from an analysis of Bergstrom, Ullio and Buckley [38] for various choices of halo profile. Bahcall *et al.* finds $\rho_S = 0.34\,\mathrm{GeV/cm^3}$ [35], Caldwell and Ostriker find $\rho_S = 0.23\,\mathrm{GeV/cm^3}$ [36] while Turner calculates $\rho_0 = 0.3 - 0.6\,\mathrm{GeV/cm^3}$ [37].

1.4.2 Galactic substructures

Simulation predict a DM distribution as a sum of a smooth halo component, and of an additional clumpy one with total masses roughly of the same order of magnitude. Hereafter we will assume for the mass of the Milky Way $M_{\mathrm{MW}} = M_{\mathrm{h}} + M_{\mathrm{cl}} = 2 \times 10^{12} M_\odot$, where M_{h} and M_{cl} denote the total mass contained in the host galactic halo and in the substructures (subhaloes)

distribution, respectively. The relative normalization is fixed by imposing that the total mass in subhaloes, whose mass ranges between $10^7 M_\odot$ and $10^{10} M_\odot$, amounts to 10% of $M_{\rm MW}$ [30]. Current numerical simulations can resolve clumps with a minimum mass scale of $\sim 10^7 M_\odot$. However, for WIMP particles (see next chapter), clumps down to a mass of $10^{-6} M_\odot$ are expected [40, 41] . We will thus consider a clump mass range between $10^{-6} M_\odot$ and $10^{10} M_\odot$.

Finally, to fully characterize the subhalo population we will assume a mass distribution $\propto m_{cl}^{-2}$ and that they are spatially distributed following the NFW profile of the main halo, i.e. with a mass spectrum number density of subhaloes, in galactocentric coordinates $\vec{r}$, given by

$$\frac{{\rm d}n_{\rm cl}}{{\rm d}m_{\rm cl}}(m_{\rm cl}, \vec{r}) = A \left(\frac{m_{\rm cl}}{M_{\rm cl}}\right)^{-2} \left(\frac{r}{r_h}\right)^{-1} \left(1 + \frac{r}{r_h}\right)^{-2} \ , \tag{1.11}$$

where A is a dimensional normalization constant. Recent results show that mass distribution seems to converge to $m_{\rm cl}^{-1.9}$ rather than $m_{\rm cl}^{-2}$. However, with a minimum mass scale of $10^{-6} M_\odot$, an mass index of 2.0 or 1.9 produces only a minor change in the following results. A more realistic clump distribution should take into account tidal disruption of clumps near the galactic center. Also, numerical simulations suggest that the radial distribution could be somewhat anti-biased with respect to the host halo profile. However, with our conservative assumptions the host halo dominates the DM annihilation signal until $20^\circ - 30^\circ$ from the galactic center so that the details of the clumps distribution have just a slight influence on the final results.

Following the previous assumptions the total mass in DM clumps of mass between m_1 and m_2 results to be

$$\begin{aligned} M(m_1, m_2) &= \int {\rm d}\vec{r} \int_{m_1}^{m_2} m_{\rm cl} \frac{{\rm d}n_{\rm cl}}{{\rm d}m_{\rm cl}}(m_{\rm cl}, \vec{r}) {\rm d}m_{\rm cl} \\ &= 4\pi \left[\ln(1 + c_h) - \frac{c_h}{1 + c_h}\right] \left(A\, r_h^3\, M_{\rm cl}\right) \ln\left(\frac{m_2}{m_1}\right) M_{\rm cl} \ , \end{aligned} \tag{1.12}$$

where $c_{\rm h} \equiv r_{\rm vir}/r_{\rm h}$ denotes the host halo concentration; while their number is

$$\begin{aligned} N(m_1, m_2) &= \int {\rm d}\vec{r} \int_{m_1}^{m_2} \frac{{\rm d}n_{\rm cl}}{{\rm d}m_{\rm cl}}(m_{\rm cl}, \vec{r}) \ {\rm d}m_{\rm cl} \\ &= 4\pi \left[\ln(1 + c_h) - \frac{c_h}{1 + c_h}\right] \left(A\, r_h^3\, M_{\rm cl}\right) \left(\frac{M_{\rm cl}}{m_1} - \frac{M_{\rm cl}}{m_2}\right) \ . \end{aligned}$$

In what follow we will determine A imposing the condition:

$$M(10^{n_{1'}}M_\odot, 10^{n_{2'}}M_\odot) = p_{1',2'}M_{MW} \ ,$$

$p_{1',2'}$ being the mass fraction in the range $[10^{n_{1'}}, 10^{n_{2'}}]M_\odot$. This means that

$$\frac{A}{M_{cl}^{-1}r_h^{-3}} = \left\{4\pi\left[\ln(1+c_h) - \frac{c_h}{1+c_h}\right]\ln 10\right\}^{-1} \frac{p_{1',2'}}{n_{2'}-n_{1'}}\frac{M_{MW}}{M_{cl}} \ .$$

So

$$M(m_1, m_2) = \frac{p_{1',2'}}{n_{2'}-n_{1'}}\frac{\ln(m_2/m_1)}{\ln 10}M_{MW}$$

and

$$N(m_1, m_2) = \frac{p_{1',2'}}{n_{2'}-n_{1'}}\frac{1}{\ln 10}\left(\frac{M_{MW}}{m_1} - \frac{M_{MW}}{m_2}\right) \ .$$

Following [30] we will assume $n_{1'} = 7$, $n_{2'} = 10$ and $p_{1',2'} = 10\%$. This means that

$$\frac{p_{1',2'}}{n_{2'}-n_{1'}} = \frac{1}{30} \ .$$

Using this condition we can calculate the mass due to the entire clumps distribution: $[10^{-6}, 10^{10}]M_\odot$:

$$M_{cl} = M(10^{-6}M_\odot, 10^{10}M_\odot) = \frac{16}{30}M_{MW} \sim 53.3\,\%M_{MW} \ ,$$

while for the number of these clumps we obtain

$$N(10^{-6}M_\odot, 10^{10}M_\odot) = \frac{10^6}{30\ln 10}\frac{M_{MW}}{M_\odot} \sim 2.90\times 10^{17} \ .$$

Finally by using the previous constraints one can fix the values of free parameters r_0 and ρ_0. Thus we solve

$$\begin{aligned} M_{vir} &= \frac{14}{30}M_{MW} = M_{\rm h} \ , \\ \rho(R_S) &= \rho_S \ , \end{aligned}$$

jointly with the equation defining the virial mass:

$$\frac{M_{vir}}{\frac{4}{3}\pi r_{vir}^3} = \Delta\rho_{cr} \quad (\Delta = 200) \ ;$$

hence obtaining $r_0 = 14.0$ kpc and $\rho_0 = 0.572$ GeVc^{-2}cm^{-3}.

A further piece of information is required to derive the annihilation signal from the clumps, namely how the DM is distributed inside the clumps themselves. We will assume that each clump follows a NFW profile as the main halo with $r_{\rm cl}$ and $\rho_{\rm cl}$ replacing the corresponding quantities of Eq. (1.9). However, for a full characterization of a clump, further information on its concentration $c_{\rm cl}$ is required. Unluckily, numerical simulation are not completely helpful in this case, since we require information about the structure of clumps with masses down to $10^{-6}M_{\odot}$, far below the current numerical resolution. Analytical models are thus required. In the current cosmological scenario [1] structures formed hierarchically, *via* gravitational collapse, with smaller structures forming first. Thus, naively, since the smallest clumps formed when the universe was denser, a reasonable expectation is $c_{\rm cl} \propto (1 + z_f)$, where z_f is the clump formation redshift. Following the model of ref. [42] we will thus assume $c_{\rm cl} = c_1 \left(\frac{m_{\rm cl}}{M_{\odot}}\right)^{-\alpha}$ with $c_1 = 38.2$ and $\alpha = 0.0392$. With this concentration the integrated DM annihilation signal from all the substructures dominates over the smooth halo component only at about 30° from the galactic center (see chapter 3), so that the constraints on the DM signal do not crucially depend on the unresolved clumps signal, coming basically only from the smooth halo component. However, given the large uncertainties in the models, larger contributions from the unresolved population of clumps are in principle possible considering a different parametrization of the concentration (see for example the various models considered in [43, 32]). We will not investigate further this possibility here.

1.5 Galactic Magnetic Field

The observation of linear polarization of starlight in 1949 constituted the first evidence for the presence of a magnetic field filling our Galaxy [44]. Following measurements, taking advantage from various different phenomena – as the *Zeeman spectral-line splitting* and the *Faraday rotation*[1] of the lin-

[1]Effect firstly discovered by Michael Faraday passing polarized light through glass in presence of a magnetic field. It consist in the rotation of the vector field of a polarized wave due to the presence of electrons and a magnetic field along its path. It can be understood in this way. The linearly polarized wave makes the electron vibrate parallel to the electric field of the wave At the same time the steady magnetic field that is present is trying to make the electron go round in circles. As a result the polarization of the wave is twisted. The amount of Faraday rotation is less the shorter the wavelength. By observing the direction of polarization at different wavelengths, it is possible to derive valuable information about electron densities and magnetic fields encountered along the path of the wave. Such studies also enable to unravel the initial direction of polarization of the emitted wave, and hence deduce the orientation of the magnetic field at the source.

early polarized radio signal emitted by pulsars – confirmed the first hint and contributed to our present, and unfortunately very partial, knowledge of the structure of the Galactic magnetic field (GMF).

Several assumptions on the global structure of the GMF are actually based on the observations of other spiral galaxies (mainly using the Faraday rotation measurement) or from hypothesis of the mechanisms of magnetic field generation (for example the galactic dynamo model).

The main characteristic of the GMF is that it seems to be the superposition of two components: regular and turbulent. [45] The turbulent, random, component posses a typical length scale of $50 \div 150$ pc, while the typical scale of the regular component is the kpc. Also, the intensity of the turbulent component is about two or three time the intensity of the regular component.

Following [46, 47, 48], we can resume the main features of the GMF in the following points:

- The intensity of the total field (regular plus turbulent components) is about 6 ± 2 μG in the disk and 10 ± 3 μG within 3 kpc from the Galactic center.

- The local regular component is mainly present in the regions between the optic arms, so its pattern resembles the two spiral arms of the luminous matter. It posses different properties in the disk and the halo. In the disk, the field is essentially toroidal, i.e. only its radial (B_r) and azimuthal (B_θ) components are non-vanishing. Its intensity is about 4 ± 1 μG. In particular, the local Galactic field is oriented mainly parallel to the plane, with a vertical component of only $B_z \simeq 0.2 \div 0.3$ μG in vicinity of the Sun. The recent explanation is that this component is present due to existence of poloidal magnetic field.

- Two field reversals – the first between the Local and Sagittarius arm, at ~ 0.6 kpc from the Sun, the second one at ~ 3 kpc from the Sun. – exist in the direction towards Galactic center. They were confirmed recently.

- The Galactic center region contains highly regular magnetic fields with strengths up to 1 mG. This extremely intensive field is concentrated in thin filaments oriented perpendicularly to the Galactic plane. The characteristic length of these filaments is about 0.5 kpc.

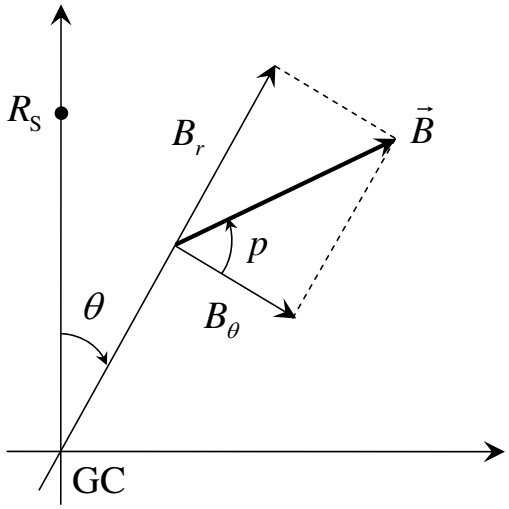

Figure 1.5: The pitch angle.

- The Galaxy is surrounded by a thick radio disk (height of about 1.5 kpc above and under Galactic plane, half-width of 300 pc) similar to that of the edge-on spiral galaxies. The field strength in this thick disk is about 1 μG. The most common explanation of existence of such thick disc is that this field is toroidal field originating through some dynamo effect.

- The local Galactic field in the standard thin disk has an even symmetry with respect to the plane (it is a quadrupole). This property, too, is in the agreement with the galactic dynamo model.

Due to the lack of knowledge about the turbulent component, in our calculations the only regular component will be taken into account.

Naively, the random component is expected to affect the synchrotron maps that we will show in the following producing a blurring of the otherwise regular pattern. Also, the random component contributes to increase the overall normalization of the field. Thus without this component the synchrotron signal is slightly underestimated so that we can regard this choice as conservative.

So let's concentrate on the regular component only. In Galactocentric cylindrical coordinates, the field components in the disk can be parameterized as

$$B_r = B(r,\theta)\sin p\,, \qquad B_\theta = B(r,\theta)\cos p\,, \tag{1.13}$$

where p is the pitch angle (see figure 1.5). Estimates for the pitch angle are $p = -8^\circ \pm 2^\circ$ from pulsar [49] and starlight polarization data, but other

observations pointing to a value of $p \simeq -13^\circ \div -18^\circ$ also exist [50]. Our choice is $p = -8^\circ$.

The function $B(r, \theta)$ is traditionally modeled reminiscent of the spiral structure of the matter distribution in the Galaxy as

$$B(r, \theta) = b(r) \cos\left(\theta - \frac{1}{\tan p} \ln(r/\xi_0)\right) . \tag{1.14}$$

In terms of the distance d to the closest sign reversal, ξ_0 can be expressed as

$$\xi_0 = (R_S + d) \exp(-\frac{\pi}{2} \tan p) ,$$

where $R_S \simeq 8.5$ kpc is the Galactocentric distance of the Sun and d is fixed to -0.5 kpc. The radial profile function $b(r)$ is generally assumed to fall off as $\propto r^{-1}$ [51, 52], consistent with pulsar measurements [53].

The behavior of the disk field in the inner region of the Galaxy is less known, but clearly the field can not diverge for $r \to 0$. For $r \geq r_{\rm max}$, the field is turned off. In the following, we will fix $r_{\rm max} = 20$ kpc.

Despite remaining uncertainties, the regular magnetic field in the thin disk is yet much better known than other components, namely the halo (or thick disk) field and a possible dipole field. The first one could dominate at large Galactic latitudes and the second one may be of crucial importance near the center of the Galaxy.

For the halo field, an extrapolation of the thin disk field into the Galactic halo with a scale height of a few kpc has often been assumed (e.g. [51, 52]). This minimal choice is in agreement with radio surveys of the thick disk [54] and mimics the expected behavior of a "Galactic wind" diffusing into the halo. However, Faraday rotation maps [49, 55] of the inner Galaxy ($-90^\circ < l_G < 90^\circ$) and of high latitudes ($|b_G| > 8^\circ$) favor a roughly toroidal component in the halo, of opposite sign above and below the plane (odd z parity or configuration A) and with an intensity of 1–2 μG [56]. Moreover, there is some evidence for a B_z component of about $0.2\,\mu$G at the Sun distance [57] that could derive from a dipolar structure at the GC [58]. In the filaments already detected, the field strength almost reaches the mG scale [50].

Recent analyses [59, 60] including new available data seems to favor the presence of these further structures. Despite this fact we will simply model the vertical profile of the field outside the plane $z = 0$ by

$$B(r, \theta, z) = f(z) B(r, \theta) .$$

So, to fully characterize the regular component of the GMF the only thing left to do is to assign the functions $b(r)$ and $f(z)$. We will follow the simple

model adopted by Tinyakov and Tkachev [52], so we assume $b(r) \propto r^{-1}$ for $r > r_{\rm min} = 4$ kpc, and $b(r) = \text{const.}$ for $r \leq r_{\rm min}$. The field $b(r)$ is normalized to 1.4 μG at the Solar position. This model has an exponential suppression law to describe the field outside the disk:

$$f(z) = \text{sign}(z) \exp(-|z|/z_0) \ ,$$

being $z_0 = 1.5$ kpc chosen as the typical halo size.

This is the GMF model we adopt in the following. It is depicted in fig. 1.5.

1.6 The Interstellar Radiation Field

The Galactic interstellar radiation field (ISRF) plays a fundamental role in the propagation of electrons, via the inverse Compton effect. We use the detailed model adopted by the Galprop propagation code, fully described in [61]. It uses a model for the distribution of stars within the Galaxy based on the statistical SKY model of Wainscoat and collaborators [62], with updates to better match recent observations and theoretical advances in stellar spectral modeling (see references therein for a detailed list of the improvements made).

The light emitted by stars is absorbed and scattered by dust in the interstellar medium (ISM). Absorbed light is re-emitted in the infra-red, while scattered light undergoes further absorption and scattering. To calculate the dust extinction (absorption and scattering), and diffuse infra-red emission, a model for dust in the ISM is required. It is assumed to follows the Galactic gas distribution described in [63].

The model assumes a cylindrical geometry for the radiation field calculation, and the calculations are simplified by adopting symmetry about the Galactic plane and in azimuth. The maximum radial extent of the Galactic volume is taken to be 20 kpc, and the maximum height above the plane z_{max} is set equal to 5 kpc.

The optical radiation field is then obtained following the method of Kylafis and Bahcall [64]. The optical radiation field for absorption only (no scattering) is calculated first. This radiation field is then used as input to calculate the amount of light scattered only once. The 'once-scattered' radiation field is used as input to calculate the amount of light scattered twice, and so forth. Absorption with the contribution by once- and twice-scattered light is found to be the only relevant contributes, so the total optical radiation field is obtained by summing them.

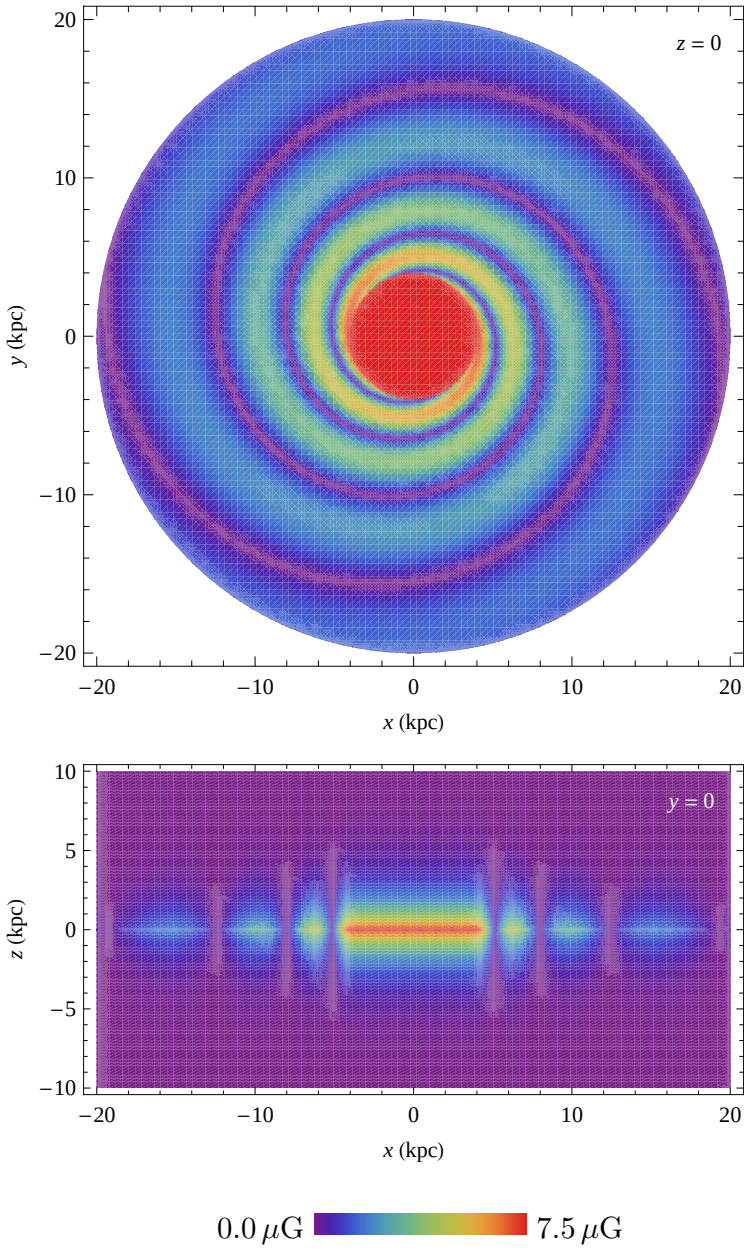

Figure 1.6: Projections of the GMF intensity in the xy and xz planes. The field reaches its highest value inside the 8 kpc–wide region at the Galactic center, where $B = 7.12$ μG.

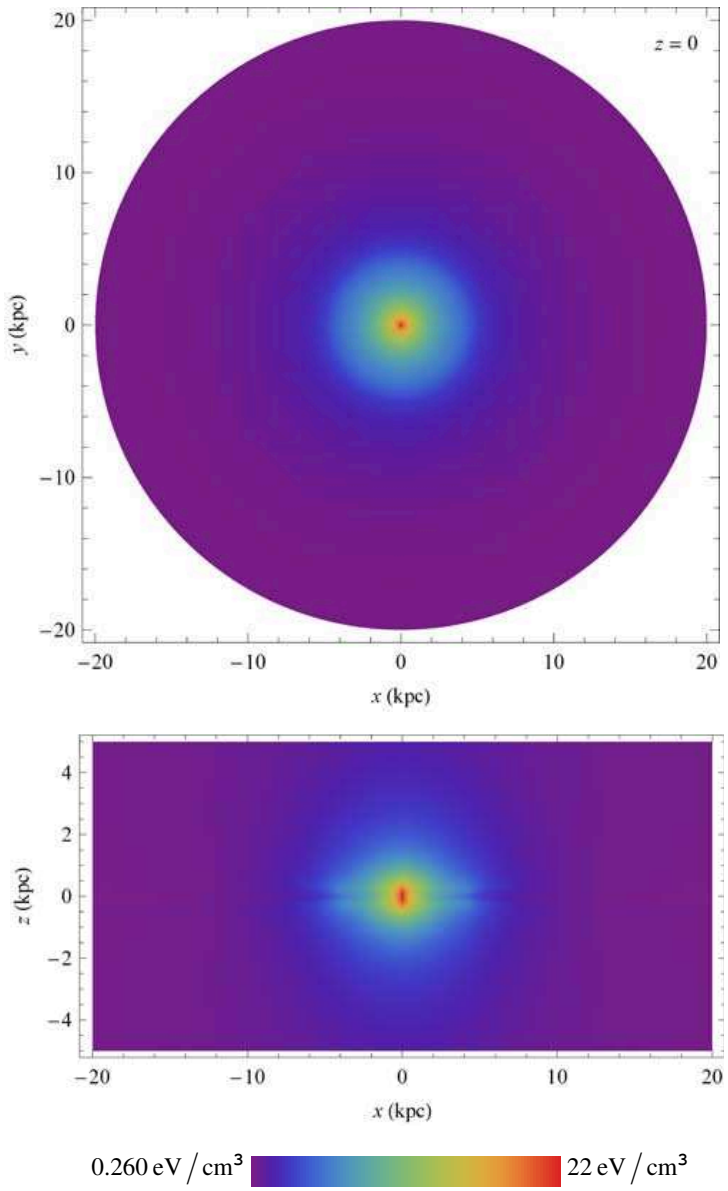

Figure 1.7: Projections of the ISRF intensity in the xy and xz planes. The lesser endpoint of the energy density scale corresponds to the pure CMB photons background.

The infra-red radiation field is obtained by using the total optical radiation field to calculate the emissivity for transient and equilibrium heating. Subsequently, the infra-red radiation field is used to calculate the re-absorbed infra-red emissivity. The total infra-red radiation field is the sum of these two components.

The resulting field intensity is represented in Fig. 1.5, that shows two projections of the ISRF in the xy and xz planes.

Chapter 2

Weakly interacting massive particles. The neutralino

As we saw in the previous chapter the matter density in the universe point to a value larger than the maximal value provided by baryons alone, according to Big Bang nucleosynthesis (BBN) [65] and confirmed by WMAP data [1]. The need for nonbaryonic dark matter is therefore striking.

An important task of cosmology and particle physics is to produce viable non-baryonic candidates. An alternative approach to the introduction of new particles in the theory could obviously be the modification of the gravitational theory itself, but it has turned out to be very difficult to modify gravity on the various length scales where the dark matter manifests its presence. Till now only the flatness of galaxy rotation curves seems to be easily explainable by introducing violations of Newton's laws [66].

Therefore the topic of this chapter will be the theoretical justification of the nowadays common belief that a huge amount of non standard particles exists. Also, there is a fascinating coincidence of characteristics these particles have to posses to both solve the dark matter problem and be naturally exhibited by the most probable extension of the Standard Model of particle physics. To understand how this happens we will firstly approach the problem from a cosmological point of view. Therefore, we will introduce a new particle specie into the primordial plasma of particles constituting the early universe and follow the evolution of its density during the expansion that followed the Big Bang.

2.1 Thermal relics

We can describe the early universe as a thermal bath of particles at equilibrium, due to the hight rate of their mutual interactions. However, these interactions have to be frequent enough to resist to the expansion effect that would lead each specie of particle out of the equilibrium. This is intuitive interpretation we can give to the Boltzmann transport equation,

$$\frac{\mathrm{d}n}{\mathrm{d}t} = -3Hn - \langle\sigma_A v\rangle(n^2 - n_{eq}^2) \ , \tag{2.1}$$

describing the evolution of the number density $n(t)$ of the particular specie we are considering. H is the Hubble expansion rate and $\langle\sigma_A v\rangle$ is the thermally averaged total cross section for annihilation into lighter particles times the relative velocity v. The reason why we are considering only lighter particles is that in what follows we will refer to massive particles possessing non relativistic velocity. Therefore we can consider them practically at rest respect to their annihilation products. Relativistic dark matter particles, in fact, do not seem to be able to drive the primordial inhomogeneities of the baryonic matter distribution towards the structures we observe today. So we will restrict our study to non relativistic, often called *cold*, dark matter. At last, n_{eq} is the number density at thermal equilibrium hence, for a massive particle, it can be written as the integral of a Maxwell–Boltzmann distribution:

$$n_{eq} = g\left(\frac{mT}{2\pi}\right)^{3/2} e^{-m/T} \ , \tag{2.2}$$

g being the number of degrees of freedom of the particle. For example, in the case of a spin–1/2 charged particle moving through a magnetic field, $g = 2$ and corresponds to the two possible values of the spin.

Equation (2.1) can be easily interpreted in this way:

1) The $-3Hn$ term represents the reduction to the particle density number due to the expansion effect. In fact, neglecting the interactions ($\sigma_A = 0$) the Boltzmann equation reduces to

$$\frac{\mathrm{d}n}{\mathrm{d}t} = -3Hn \ .$$

Remembering that $H = \dot{a}/a$ we obtain

$$\frac{\mathrm{d}n}{n} = -3\frac{\dot{a}}{a}\mathrm{d}t = -3\frac{\mathrm{d}a}{a} \ ,$$

that leads us to the expected result, $n(t) \propto a^{-3}(t)$, that the number density n decreases only due to the expansion effect.

2) The $-\langle\sigma_A v\rangle n^2$ term is the number of particles that, annihilating, reduce n.

3) At last, the $+\langle\sigma_A v\rangle n_{eq}^2$ represents the creation of new particles due to the inverse creation process.

Equation (2.1) does not admit analytic solutions. Nevertheless very accurate approximated solutions can be obtained. We will not report here the way they are deduced, because this is very well explained elsewhere [67]. We will only try to make a little bit more quantitative our previous simplifying interpretation.

First of all, equation (2.1) can be recast in a more convenient way as

$$\frac{x}{Y_{eq}}\frac{dY}{dx} = -\frac{\Gamma_A}{H}\left[\left(\frac{Y}{Y_{eq}}\right)^2 - 1\right] , \tag{2.3}$$

in terms of the new variables

$$Y = \frac{n}{s} \quad \left(Y_{eq} = \frac{n_{eq}}{s}\right) \quad \text{and} \quad x = \frac{m}{T} ,$$

where s is the universe entropy density and T the equilibrium temperature. It is to say that we are using temperature instead of time to describe the evolution.

The quantity $\Gamma_A = n_{eq}\langle\sigma_A v\rangle$ is the *annihilation rate*, and Γ_A/H defines the decoupling time/temperature of our dark matter particles from the remaining species. An approximated estimate of this epoch can be obtained imposing the condition $\Gamma_A(T) = H(T)$ and leads to

$$T \approx \frac{m}{20} .$$

After this decoupling time the number density ceases to decrease following the equilibrium law (2.2) and its value freezes, approximately, to its current value. Therefore, the resulting cosmological abundance can be calculated as its value at this decoupling time, and an order of magnitude estimate gives

$$\Omega_{DM}h^2 \sim \frac{3\cdot 10^{-27}\ \mathrm{cm^3 s^{-1}}}{\langle\sigma_A v\rangle} .$$

An interesting consequence of the last equation is that massive particles which have interactions of the order of the weak interactions naturally give

contributions to the matter density of the universe of order unity, and therefore can account for the missing mass. The generic name for such a dark matter candidate is a WIMP (Weakly Interacting Massive Particle).

Under the assumption that these WIMPs constitute the dark matter particles we can use the last result to try to estimate their annihilation cross section. In fact, according to eq. 1.8, we assume

$$\Omega_{DM} = \Omega_m - \Omega_b = 0.212 \ ,$$

that leads to

$$\langle \sigma_A v \rangle = \frac{3 \cdot 10^{-27} \ \mathrm{cm^3 s^{-1}}}{\Omega_{DM} h^2} \approx 3 \cdot 10^{-26} \ \mathrm{cm^3 s^{-1}} \ . \tag{2.4}$$

We conclude this section remembering that assuming a thermal production process in the early universe, there is an upper limit to the mass of a stable relic particle [68]. This comes about because unitarity precludes the annihilation cross section of particles of mass m, spin J and relative velocity (in the center of mass frame) v from being larger than

$$4\pi \frac{2J+1}{m^2 v^2} \ .$$

Using the estimated v at freeze-out, it is found that m cannot exceed around 340 TeV. The most favored heavy dark matter candidate, the lightest supersymmetric particle, always has a mass much below this limit in the minimal models.

2.2 Departures from the standard scenario

There are many situations in which the standard method of calculating the abundance of a thermal relic fails.

Coannihilation

This case occurs when the relic particle is the lightest of a set of similar particles whose masses are nearly degenerate. In this case the relic abundance of the lightest particle is determined not only by its annihilation cross section, but also by the annihilation of heavier particles, which will later decay into the lightest [69].

Annihilation into forbidden channels

This case concerns annihilation into particles which are more massive than the relic particle. In the simplified analysis of the previous section this was considered simply as kinematically forbidden, but it can be shown [69] that if the heavier particles are only 5–15 % more massive, these channels can dominate the annihilation cross section and determine the relic abundance.

Annihilation near a pole of the cross section

This case occurs when the annihilation takes place near a pole in the cross section. This happens, for example in Z^0–exchange annihilation when the mass of the relic particle is near $m_Z/2$. A pole can also occur when the annihilating dark matter particle is nearly one-half the mass of a resonance such as J/Ψ or η [69].

Non–thermal relics

Although thermal production of stable particles is a generic, unavoidable mechanism in the Big Bang scenario, there are several additional processes possible. For instance, some very heavy particles were perhaps never in thermal equilibrium. Non-thermal production may for example occur near cosmic strings and other defects. Near the end of a period of early inflation, several mechanisms related either to the inflaton field or to the strong gravity present at that epoch could contribute to nonthermal production (see, e.g., [70]).

Charge conjugation asymmetry

The most probable dark matter particle candidates, the supersymmetric neutralino (see next section) or the lightest Kaluza–Klein particle are both self-conjugate[1], nevertheless if the particle is different from the antiparticle, it may be that there exists an asymmetry similar to that we know had to exists for the baryons that otherwise would have been quickly completely annihilated by antibaryons in the early universe. Such an asymmetry can make the relic number density of the dark matter particles higher than if there would be a perfect symmetry. This may allow for a relic density which is higher than the estimate in Eq. (2.1) even if the annihilation cross section is large. [add Ref.]

[1]It is quite obvious that dark matter has to be electrically neutral.

Evading unitarity

There may be a possibility to evade the unitarity bound showed at the end of section 2.1 and accept even extremely heavy particles as dark matter candidates if, for instance, they are not absolutely stable (so that the formula in Eq. (2.1) does not apply), or if the production mechanism is non-thermal [71, 72].

Due to the large number of phenomena that can alter the estimate 2.4 of the annihilation cross section, we will assume $\langle \sigma_A v \rangle$ as a free parameter. The same we will make with regards to the dark matter particle mass.

However, to fully calculate the radio signal produced by the annihilation we need to specify a particular particle. This will be the pretext to briefly introduce one of the most desirable solutions to the problem: the possibility that Supersymmetry not only represents the right way to extend the Standard Model of the particle physics but, also, that its lightest particle, in many cases a neutralino, is the particle we are looking for. This will be the subject of the second part of this chapter.

2.3 Supersymmetry

A review of the supersymmetric theories is obviously out of the scope of a thesis devoted to the indirect detection of dark matter. Therefore, in the following pages, I will simply remember to the reader what were the main reasons that lead to its formulation. I will also introduce only the unavoidably concepts and definitions needed to introduce the dark matter candidate I will consider in the following chapters, the so–called neutralino. For further discussions of supersymmetry, we refer the interested reader to Refs. [73, 77, 78, 79, 3, 80, 81, 82].

As we know, in the Standard Model of particle physics there exists a fundamental distinction between bosons and fermions: bosons are the mediators of interactions, while fermions are the constituents of matter. One of the main achievements of supersymmetry is to provide a unified picture of matter and interactions.

We know that the elementary fermions constitute the irreducible representations of the Poincaré group, while bosons are introduced into the theory according to the gauge principle. Hence the entire Standard Model particles spectrum comes out from the assumptions of the invariance of the theory under a symmetry group which is the product of the Poincaré group by the internal/gauge group. Therefore a possible way to wipe out the previous di-

chotomy is to ask whether a Lie group exists mixing internal and space-time symmetries. Early attempts to find such a group had to face the limitations imposed by the so–called *no-go* theorem of Coleman and Mandula [84]. Such limitations were avoided at last introducing new fermionic generators satisfying anticommutation relations instead of the usually assumed commutation relations of the quantum theory. Such, mixed algebras, were called *graded* Lie algebras. They include generators that change fermions into bosons and vise versa:

$$Q\,|\text{fermion}\rangle = |\text{boson}\rangle\,; \quad Q\,|\text{boson}\rangle = |\text{fermion}\rangle\,.$$

Due to their fermionic nature, the operators Q carry spin 1/2, which implies that supersymmetry must be a spacetime symmetry. The question then arises of how to extend the Poincaré group of spatial translations and Lorentz transformations to include this new boson/fermion symmetry. The structure of such a group is highly restricted by the Haag-Lopuszanski-Sohnius extension of the Coleman and Mandula theorem[85]. For realistic theories, the operators, Q, which we choose by convention to be Majorana spinors, must satisfy

$$\{Q_a, \overline{Q}_b\} = 2\gamma^\mu_{ab} P_\mu \qquad \{Q_a, P_\mu\} = 0 \qquad [Q_a, M^{\mu\nu}] = \sigma^{\mu\nu}_{ab} Q^b$$

where

$$\overline{Q}_a \equiv \left(Q^\dagger \gamma_0\right)_a \qquad \text{and} \qquad \sigma^{\mu\nu} = \frac{i}{4}[\gamma^\mu, \gamma^\nu]$$

are the structure constants of the theory.

There are also other important reasons for introducing supersymmetry. The solution it provides to the *hierarchy problem* is among the most important of these. The hierarchy problem has to do with the enormous difference between the electroweak and Planck energy scales. This problem arises in the radiative corrections to the mass of the Higgs boson. It is well known that scalar masses get radiative corrections quadratically with energy, while fermion masses increase only logarithmically. Therefore when we consider the radiative corrections at 1-loop for the Higgs boson we find

$$\delta m_H^2 \sim \left(\frac{\alpha}{2\pi}\right)\Lambda^2, \tag{2.5}$$

where Λ is a cut-off energy where new physics is expected to intervene. The Higgs mass is expected to be of the same order of the electroweak scale, it to say that $m_H \sim 100$ GeV, while its radiative correction can be order TeV if Λ is about the Planck mass. This clearly destroy the stability of the electroweak scale.

A possible solution to this problem is to assume the existence of new particles with similar masses but opposite statistics. Then, since the contribution of fermion loops to δm_s^2 have a famous opposite sign to the corresponding bosonic loops, at the 1-loop level, Eq. (2.5) becomes

$$\begin{aligned} \delta m_s^2 &\sim \left(\frac{\alpha}{2\pi}\right)\left(\Lambda^2 + m_H^2\right) - \left(\frac{\alpha}{2\pi}\right)\left(\Lambda^2 + m_F^2\right) \\ &= \left(\frac{\alpha}{2\pi}\right)\left(m_H^2 - m_F^2\right). \end{aligned}$$

Providing that $|m_B^2 - m_F^2| \lesssim 1$ TeV the divergence to the Higgs mass is canceled at all orders of perturbation theory. The algebra of supersymmetry we introduced naturally guarantees the existence of new particles associated to all of the particles of the Standard Model with the same mass but opposite statistic, therefore gives a natural solution to the hierarchy problem.

A third, fundamental reason for introducing Supersymmetry comes from Grand Unification Theory, which predicts the unification of the three gauge couplings below the Planck scale. It is well known that this does not happen for the Standard Model only (fig. 2.1(a)) while, once Supersymmetry is taken into account [83] happens at a unification scale of 2×10^{16} GeV (fig. 2.1(b))

2.4 Minimal Supersymmetric Standard Model

In the following I will only consider the simplest possible way to extend the Standard Model to a supersymmetric theory. This extension constitutes the so–called Minimal Supersymmetric Standard Model (MSSM), a theory containing all the known fields of the Standard Mode, an extra Higgs doublet and the partners of the ordinary particles required to form the supersymmetric multiplets. The MSSM is clearly assumed to be invariant under the gauge group of the Standard Model, $SU(3) \times SU(2) \times U(1)$, it is required to be renormalizable and it is constrained by an additional symmetry, the R *parity*, necessary to prevent lepton and baryon number variations during the interactions.

Despite the fact that MSSM constitutes, as stated, the simplest supersymmetric description for the elementary particles interactions, it represents nevertheless an extremely difficult theory, defined by a great number of free parameters. The only fast way to deduce the lagrangian describing the MSSN makes an extensive use of the *superspace* formalism, so I will not reproduce that results here. The interested reader is redirected to the literature, where very good reviews exists on it (see for example [3, 80]). Let us only state that the superspace plays in supersymmetric theories the same role played by the

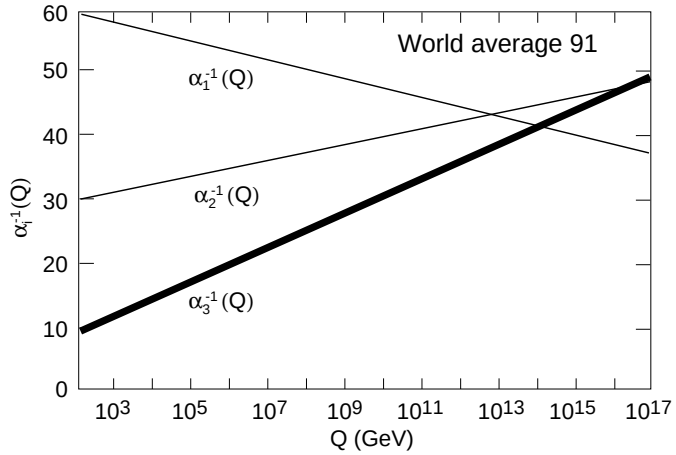

(a)

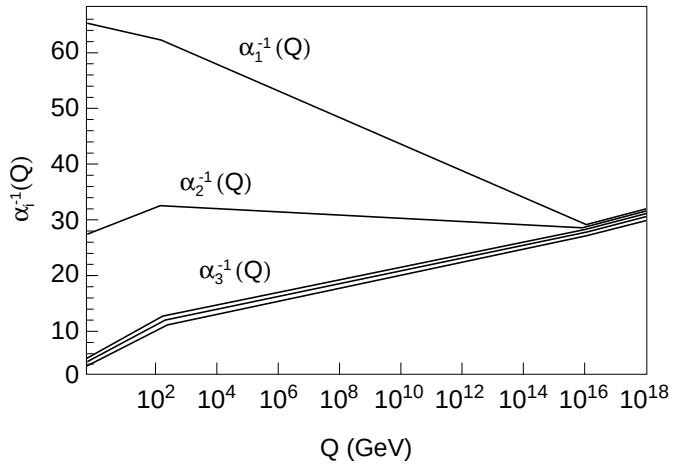

(b)

Figure 2.1: The measurements of the gauge coupling strengths at LEP do not (a) evolve to a unified value if there is no supersymmetry but do (b) if supersymmetry is included [83, 100].

Minkowsky space–time in Special Relativity, in the sense that it constitute the right formalism to make supersymmetry invariance recognizable at sight.

Given our interest in dark matter, the new ingredient of the theory we are most interested in is R parity. It constitutes a discrete symmetry whose

Standard Model particles and fields		Supersymmetric partners			
		Interaction eigenstates		Mass eigenstates	
Symbol	Name	Symbol	Name	Symbol	Name
$q = d, c, b, u, s, t$	quark	$\tilde{q}_L$, $\tilde{q}_R$	squark	$\tilde{q}_1$, $\tilde{q}_2$	squark
$l = e, \mu, \tau$	lepton	$\tilde{l}_L$, $\tilde{l}_R$	slepton	$\tilde{l}_1$, $\tilde{l}_2$	slepton
$\nu = \nu_e, \nu_\mu, \nu_\tau$	neutrino	$\tilde{\nu}$	sneutrino	$\tilde{\nu}$	sneutrino
g	gluon	$\tilde{g}$	gluino	$\tilde{g}$	gluino
$W^\pm$	W-boson	$\tilde{W}^\pm$	wino	$\tilde{\chi}^\pm_{1,2}$	chargino
H^-	Higgs boson	$\tilde{H}_1^-$	higgsino		
H^+	Higgs boson	$\tilde{H}_2^+$	higgsino		
B	B-field	$\tilde{B}$	bino	$\tilde{\chi}^0_{1,2,3,4}$	neutralino
W^3	W^3-field	$\tilde{W}^3$	wino		
H_1^0	Higgs boson	$\tilde{H}_1^0$	higgsino		
H_2^0	Higgs boson	$\tilde{H}_2^0$	higgsino		
H_3^0	Higgs boson				

Table 2.1: Standard Model particles and their superpartners in the MSSM.

action on the component fields of the theory is

$$R = (-1)^{3(B-L)+2S} ,$$

where B and L are respectively the baryon and the lepton number operators while S is the spin. It is easily recognized that R is always equal to one for the standard particle while it assumes value minus one for the supersymmetric particle, due to their opposite statistic. Consider for example an electron. In this case $L = 1$, $B = 0$, and $S = 1/2$, therefore $R = (-1)^{-2} = +1$. An hypothetical spin–0 partner of the electron would have $R = (-1)^{-3} = -1$. Such a reasoning is true for all Standard Model particles, as the reader can easily check. The assumption that R parity is the symmetry associated to a multiplicative quantum number introduces an important rule to prevent the decay of the lightest supersymmetric particle (LSP). In fact a decaying particle with $R = -1$ have to produce an even number of non standard particle. Nevertheless the LSP cannot do this, so it is stable and the only way it can change its number is annihilating in couples. This is the reason why Supersymmetry is so important in the cosmology of dark matter: it provides in a very natural way a viable dark matter candidate.

Once the degrees of freedom of the Standard Model are doubled by the introduction of a fermionic degree of freedom for each boson of the theory and by two bosons (one for the left helicity and another one for the right elicits) for each fermion, the resulting spectrum of particles appears very reach. It is reassumed in table 2.4. The most exotic features comes for the Higgs

sector. After the spontaneous electroweak symmetry breaking the MSSM possesses five Higgs bosons, three neutral and two charged: h^0, H^0, A^0, H^+, H^-. There are also presents the superpartners of the interaction states of the Higgs particles, $\tilde{H}^{\pm}$ and $\tilde{H}^0_{1,2}$ and the superpartners of the electroweak gauge bosons, $\tilde{W}^{\pm}$, $\tilde{B}$ and $\tilde{W}_3$. The charged Higgs superpartners share the same quantum number, therefore they merge to forme the mass eigenstates know as *charginos*, $\tilde{\chi}^{\pm}_{1,2}$. In the same way the neutral Higgs superpartners and the neutral gauge bosons superpartners (all fermions) form the *neutralinos*, $\tilde{\chi}^0_{1,\ldots,4}$ (ordered with increasing mass). The importance of the neutralino basically resides in the fact that the lighter of them, $\tilde{\chi}^0_1$, simply denoted χ and called *the* neutralino, is the LSP in many realizations (read parameters choice) of the MSSM.

2.5 The lightest neutralino

In the basis $(\tilde{B}, \tilde{W}_3, \tilde{H}^0_1, \tilde{H}^0_2)$, the neutralino mass matrix can be expressed as

$$\begin{pmatrix} M_1 & 0 & -M_Z \cos\beta \sin\theta_W & M_Z \sin\beta \sin\theta_W \\ 0 & M_2 & M_Z \cos\beta \cos\theta_W & -M_Z \sin\beta \cos\theta_W \\ -M_Z \cos\beta \sin\theta_W & M_Z \cos\beta \cos\theta_W & 0 & -\mu \\ M_Z \sin\beta \sin\theta_W & -M_Z \sin\beta \cos\theta_W & -\mu & 0 \end{pmatrix} .$$

The MSSM parameters intervening in the neutralino sector are therefore:

M_1, a *bino* $(\tilde{B})$ mass parameter;

M_2, a *wino* $(\tilde{W}_3)$ mass parameter;

μ , the so–called *higgsino mass term;*

$\tan\beta$, the ratio of the vacuum expectation values of the Higgs bosons.

At last, as usually made in the literature devoted to the cosmological implications of the MSSM, we will assume a relation between M_1 and M_2 that comes from Grand Unification Theory:

$$M_1 = \frac{5}{3} M_2 \tan^2\theta_W \ .$$

This permits us to reduce the neutralino MSSM parameters to three. Also, the neutralino mass is quite insensitive to $\tan\beta$, so we can fix a value for it, for example $\tan\beta = 2$ in fig. 2.5, and only care about M_2 and μ.

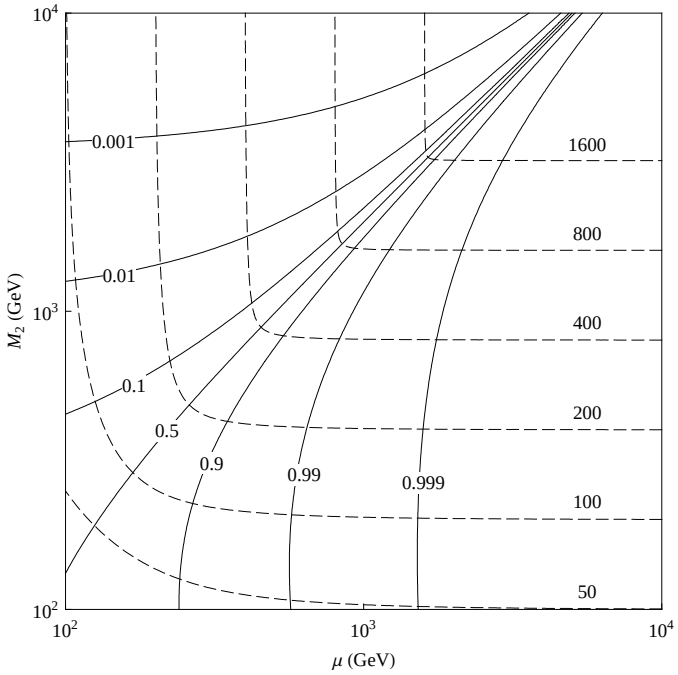

Figure 2.2: Contour plots of the neutralino mass (dashed lines) and its gaugino fraction (continuous lines). $\tan\beta = 2$ is assumed.

Writing the lightest neutralino as

$$\chi = N_{11}\tilde{B} + N_{12}\tilde{W}_3 + N_{13}\tilde{H}_1^0 + N_{14}\tilde{H}_2^0$$

we can define the *gaugino fraction*, f_G, and the *higgsino fraction*, f_H, as

$$f_G = N_{11}^2 + N_{12}^2$$

and

$$f_H = N_{13}^2 + N_{14}^2 \ .$$

The reason why we define this quantities is that the annihilation and scattering properties of the neutralino are extremely simplified if expressed in term of this fractions, while they appears extremely involved when described in terms of the pure MSSM parameters. A plot will a good examples of this.

Fig. 2.5 represents the contour plots of the neutralino mass (dashed lines), each labeled with the corresponding mass in GeV) and its gaugino fraction (continuous lines). Masses from 50 GeV till 1600 GeV are represented. The figure clearly shows that randomly choosing a couple M_2–μ the probability of obtaining a mixed neutralino, $f_G \sim f_H \sim 1/2$ is quite low. The most probable situations correspond in fact to an almost pure *higgsino*, $f_G \leq 0.1$

or an almost pure *gaugino* $f_G \geq 0.9$. This is a very fortunate case, because explicit calculation of the annihilation cross section [86], and therefore of the neutralino cosmological abundance, show that mixed neutralinos have no chances to significantly contribute to the dark matter abundance. On the contrary, low mass ($m_\chi < 100$ GeV) higgsinos and high mass ($m_\chi > 100$ GeV) gauginos are perfect candidates.

All this suggests that the attention devoted in literature to neutralino is definitely motivated.

Chapter 3

DM Synchrotron Signal

3.1 Particle Physics

As we saw in the previous chapter, in a standard scenario, where WIMPs experience a non exotic thermal history, a typical mass range for these particles is $50\,\mathrm{GeV} \lesssim m_\chi \lesssim 1\,\mathrm{TeV}$, while a simple estimate for their (thermally averaged) annihilation cross section yields $\langle \sigma_\mathrm{A} v \rangle = 3 \times 10^{-27} \mathrm{cm}^3 \mathrm{s}^{-1} / \,\Omega_c h^2$ [3], giving $\langle \sigma_\mathrm{A} v \rangle \approx 3 \times 10^{-26} \mathrm{cm}^3 \mathrm{s}^{-1}$ for $\Omega_c h^2 \approx 0.1$ as resulting from the latest WMAP measurements [1]. However, we already saw how this relation can fail badly, therefore a much wider range of cross sections should be considered viable. In this work we consider values of m_χ from 35 to 800 GeV, and $\langle \sigma_\mathrm{A} v \rangle$ in the range $(10^{-26}$-$10^{-21})\mathrm{cm}^3\mathrm{s}^{-1}$

The e^+e^- annihilation spectrum for a given super-symmetric WIMP candidate can be calculated for example with the DarkSusy package [**?**]. Fig. 3.1 shows three of these spectra, representing the most important annihilation modes for a 100 GeV neutralino: $c\bar{c}\,, b\bar{b}\,, \tau^+\tau^-\,, W^+W^-\,, Z^0Z^0$. The annihilation spectra into $b\bar{b}$ and Z^0Z^0 are not depicted, the first being extremely similar to the $c\bar{c}$ case, the second to W^+W^-. In principle the $t\bar{t}$ channel is also relevant, and very similar to the other annihilation spectra into heavy quarks, but it is forbidden due to the small mass (100 GeV) considered in the figure. Therefore, the final spectrum has only a weak dependence on the exact annihilation process with the channels $\chi\chi \to ZZ, W^+W^-, q\bar{q}$ $(q = c, b, t)$ giving basically degenerate spectra. For leptonic channels like the $\tau^+\tau^-$ decaying mode the spectrum differ significantly, although this channel has generally a quite low branching ratio. In the general case, the annihilation spectra will be simply a weighted sum of the spectra considered here.

For simplicity we will assume hereafter full decay into $q\bar{q}$ channel, hence e^- (e^+) will be emitted by decaying muons (anti-muons) produced in pions

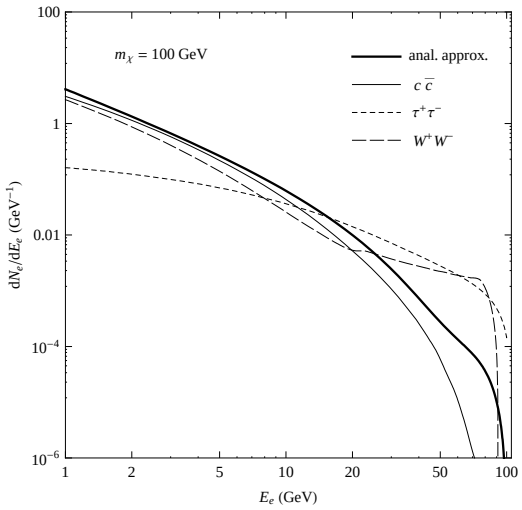

Figure 3.1: The e^+e^- spectrum from neutralino annihilations for the most important annihilation modes. Some outputs produced by DarkSusy and the analytical approximation used our calculations are compared. See text for more details.

decays. In this framework, the resulting e^+, e^- spectrum can be written as a convolution, namely

$$\frac{\mathrm{d}N_e}{\mathrm{d}E_e}(E_e) = \int_{E_e}^{m_\chi c^2} \mathrm{d}E_\mu \frac{\mathrm{d}N_e^{(\mu)}}{\mathrm{d}E_e}(E_e, E_\mu) \int_{E_\mu}^{E_\mu/\xi} \mathrm{d}E_\pi W_\pi(E_\pi) \frac{\mathrm{d}N_\mu^{(\pi)}}{\mathrm{d}E_\mu}(E_\pi) \quad (3.1)$$

with $\xi = (m_\mu/m_\pi)^2$, where

$$\frac{\mathrm{d}N_e^{(\mu)}}{\mathrm{d}E_e}(E_e, E_\mu) = \frac{2}{E_\mu}\left[\frac{5}{6} - \frac{3}{2}\left(\frac{E_e}{E_\mu}\right)^2 + \frac{2}{3}\left(\frac{E_e}{E_\mu}\right)^3\right] , \quad (3.2)$$

$$\frac{\mathrm{d}N_\mu^{(\pi)}}{\mathrm{d}E_\mu}(E_\pi) = \frac{1}{E_\pi}\frac{m_\pi^2}{m_\pi^2 - m_\mu^2} , \quad (3.3)$$

$$W_\pi(E_\pi) = \frac{1}{m_\chi c^2}\frac{15}{16}\left(\frac{m_\chi c^2}{E_\pi}\right)^{\frac{3}{2}}\left(1 - \frac{E_\pi}{m_\chi c^2}\right)^2 . \quad (3.4)$$

In particular, Eq. (3.2) is the electron (positron) spectrum produced in the muon (anti-muon) decay $\mu^- \to e^-\nu_\mu\bar{\nu}_e$ ($\mu^+ \to e^+\bar{\nu}_\mu\nu_e$). Eq. (3.3) stands for the μ^- (μ^+) spectrum from $\pi^- \to \mu^-\bar{\nu}_\mu$ ($\pi^+ \to \mu^+\nu_\mu$) decay process, and, finally, Eq. (3.4) provides a reasonable analytical approximation of the spectrum of pions from $q\bar{q}$ hadronization [**?**]. It is worth noticing that to be more

accurate Eq. (3.4) should be substituted by a numerical calculation, which however results not necessary for the aim of the present work as discussed in the following.

In this approximation the final electron (positron) spectrum can be cast in a simple polynomial form of the ratio $E_e/m_\chi c^2$ (see Appendix A):

$$\frac{\mathrm{d}N_e}{\mathrm{d}E_e}(E_e) = \frac{1}{m_\chi c^2} \sum_{j\in J} a_j \left(\frac{E_e}{m_\chi c^2}\right)^j , \tag{3.5}$$

where $J = \{-\frac{3}{2}, -\frac{1}{2}, 0, \frac{1}{2}, 2, 3\}$ and the coefficients a_j are listed in Table 3.1.

The main advantage of using the analytical approximation (3.5) instead of a more accurate numerical input is that, as will be clear in the next sections, most of the observables for the radio emission will be expressed in an analytical form as well. This would certainly implies a better understanding of physical results. Also, expression (3.5) is quite general so, for a large class of different annihilation models the only required chances concern the set J of the of the spectral indices and the coefficients a_j.

We expect that the difference with the complete numerical calculation turns to be small, with differences arising only for quite low electron energies, and thus for very low radio frequencies. At low energies, in fact, the analytical form has an asymptotic behavior $\propto E_e^{-1.5}$ while the numerical spectrum has a turn down. From a comparison with the numerical output from DarkSusy for a 100 GeV WIMP with 100% branching ratio into $b\bar{b}$ the analytical form is a fair approximation until $E_e \approx 1$ GeV, which from Eq. (3.17) (see below) for a magnetic field $B \sim 10\,\mu$G translates into a minimum valid frequency $\nu =$ 10–100 MHz, thus below the frequency window we are going to explore.

Despite the fact that we will always use the spectra (3.5) in our numerical calculations, many of the formulas will refer to the general case too. In this case the annihilation spectra can be parameterized in terms of a numerical

Table 3.1: a_j values

coefficient	**analytical**	**numerical**
$a_{-3/2}$	$\frac{65}{189}\frac{1-\xi^{3/2}}{1-\xi}$	0.456
$a_{-1/2}$	$-\frac{66}{7}\frac{1}{1+\xi^{1/2}}$	−5.37
a_0	$\frac{25}{36}\frac{\xi^2-18\,\xi+8\,\xi^{1/2}+9}{(1-\xi)\xi^{1/2}}$	10.9
$a_{1/2}$	$9\frac{1-\xi^{-1/2}}{1-\xi}$	−6.77
a_2	$-\frac{3}{28}\frac{5\,\xi^2-42\,\xi+72\,\xi^{1/2}-35}{(1-\xi)\xi^{1/2}}$	0.969
a_3	$\frac{1}{189}\frac{35\,\xi^2-270\,\xi+424\,\xi^{1/2}-189}{(1-\xi)\xi^{1/2}}$	−0.185

function $f(x)$ in the form

$$\frac{\mathrm{d}N_e}{\mathrm{d}E_e}(E_e) = \frac{1}{m_\chi c^2} f\left(\frac{E_e}{m_\chi c^2}\right). \tag{3.6}$$

Notice that $f(x)$ must fulfill the conditions $f(0) = f(1) = 0$.

3.2 Electrons equilibrium distribution

Dark matter annihilation injects electrons in the galaxy at the constant rate

$$Q(E_e, r) = \frac{1}{2}\left(\frac{\rho(r)}{m_\chi}\right)^2 \langle\sigma_{\mathrm{A}} v\rangle \frac{\mathrm{d}N_e}{\mathrm{d}E_e}\ . \tag{3.7}$$

On the other hand, the injected electrons loose energy interacting with the interstellar medium and diffuse away from the production site. In the limit in which convection and reacceleration phenomena can be neglected, the evolution of the e^+e^- fluid is described by the following diffusion-loss equation [101, 102, 103]

$$\frac{\partial}{\partial t}\frac{\mathrm{d}n_e}{\mathrm{d}E_e} = \vec{\nabla}\cdot\left[K(E_e,\vec{r})\vec{\nabla}\frac{dn_e}{dE_e}\right] + \frac{\partial}{\partial E_e}\left[b(E_e,\vec{r})\frac{\mathrm{d}n_e}{\mathrm{d}E_e}\right] + Q(E_e,\vec{r}), \tag{3.8}$$

where $\mathrm{d}n_e/\mathrm{d}E_e$ stands for the number density of e^+, e^- per unit energy, $K(E_e,\vec{r})$ is the diffusion constant, and $b(E_e,\vec{r})$ represents the energy loss rate. The diffusion length of electrons is generally of the order of a kpc (see section 3.3.1) thus for the diffuse signal generated all over the galaxy, and thus over many kpc's, spatial diffusion can be neglected. This is not the case for the signal coming from a single clump for which the emitting region is much smaller than a kpc. We will further analyze this point later.

By neglecting diffusion, the steady state solution of eq. (3.8) can be expressed as

$$\frac{\mathrm{d}n_e}{\mathrm{d}E_e}(E_e,\vec{r}) = \frac{\tau}{E_e}\int_{E_e}^{m_\chi c^2} dE'_e\ Q(E'_e,\vec{r})\,, \tag{3.9}$$

where $\tau = E_e/b(E_e,\vec{r})$ is the cooling time, resulting from the sum of several energy loss processes that affect electrons.

By inserting (3.6) and (3.7) into the last equation we get the following equilibrium distribution for electrons

$$\frac{\mathrm{d}n_e}{\mathrm{d}E_e}(E_e,\vec{r}) = \frac{\langle\sigma_{\mathrm{A}} v\rangle\,\tau(\vec{r})}{2E_e}\left(\frac{\rho(r)}{m_\chi}\right)^2\left[F(1) - F\left(\frac{E_e}{m_\chi c^2}\right)\right]\ , \tag{3.10}$$

being $F(x)$ the primitive function of $f(x)$.

When the analytic form of the spectrum, eq. (1.4), is used this result can be explicitly expressed as

$$\frac{\mathrm{d}n_e}{\mathrm{d}E_e}(E_e,\vec{r}) = \frac{\langle\sigma_{\mathrm{A}}v\rangle\,\tau(\vec{r})}{2\,m_\chi c^2}\left(\frac{\rho(r)}{m_\chi}\right)^2\sum_{k\in\mathcal{K}} b_k\left(\frac{m_\chi c^2}{\mathrm{GeV}}\right)^{-k}\left(\frac{E_{\mathrm{e}}}{\mathrm{GeV}}\right)^k, \qquad (3.11)$$

being $\mathcal{K} = J\cup\{-1\}$, $b_k = -a_k/(k+1)$, if $k \neq -1$, while $b_{-1} = \sum_{j\in J} a_j/(j+1)$.

Therefore, the only thing left to do is to calculate the cooling time $\tau(\vec{r})$. In the following we will consider synchrotron emission and inverse Compton scattering (ICS) off the background photons (CMB and starlight) only, which are the faster processes and thus the ones really driving the electrons equilibrium. Other processes, like synchrotron self absorption, ICS off the synchrotron photons, e^+e^- annihilation, Coulomb scattering over the galactic gas and bremsstrahlung are generally slower. They can become relevant for extremely intense magnetic field, possibly present in the inner parsecs of the galaxy [14], and thus will be neglected in this analysis.

For synchrotron emission the energy loss is given by (for ex. cfr. [104])

$$b_{\mathrm{syn}}(E_e) = \frac{4}{3}\,c\sigma_{\mathrm{T}}\gamma^2\beta^2 U_B$$

with $U_B = B^2/2\mu_0$ the magnetic energy density so that the time scale of the energy loss is:

$$\tau_{\mathrm{syn}} = \tau^0_{\mathrm{syn}}\left(\frac{B}{\mu\mathrm{G}}\right)^{-2}\left(\frac{E_e}{\mathrm{GeV}}\right)^{-1} \qquad (3.12)$$

with $\tau^0_{\mathrm{syn}} = 3.95\times10^{17}\mathrm{s}$.

Similarly, for Inverse Compton emission the energy loss is given by

$$b_{\mathrm{ICS}} = \frac{4}{3}\,c\sigma_{\mathrm{T}}\gamma^2\beta^2 U_{\mathrm{rad}}.$$

The relevant radiation background for ICS is given by an extragalactic uniform contribution consisting of the CMB with

$$U_{\mathrm{CMB}} = \int_0^\infty \frac{8\pi\epsilon}{h^3c^3}\left[\exp\left(\frac{\epsilon}{kT}-1\right)\right]^{-1} = \frac{8\pi^5(kT)^4}{15(hc)^3} \approx 0.26\ \mathrm{eV/cm^3}\ ,$$

the optical/infrared extragalactic background and by the analogous spatially varying galactic contribution, the Interstellar Radiation Field (ISRF). For the latter we use as template the Galprop distribution model [105] which reduces to the extragalactic one at high galactocentric distances. In this model, the ISRF intensity near the solar position is about 5 $\mathrm{eV/cm^3}$, and

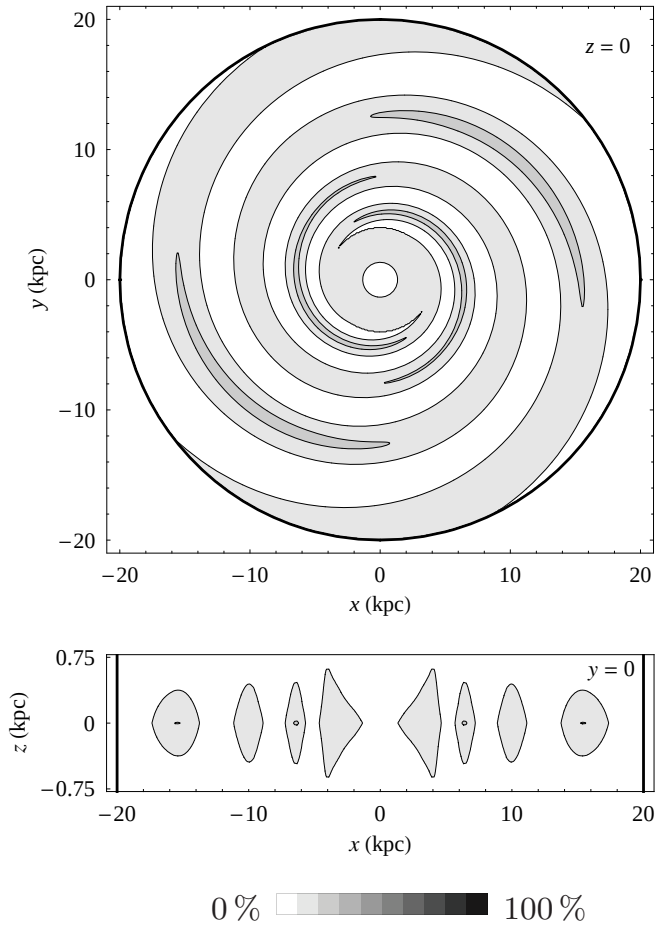

Figure 3.2: Projections of the galaxy in the xy and xz planes showing the fractional synchrotron contribution to the e^+e^- total energy losses for TT model [52] of GMF and Galprop model [105] of ISRF. The synchrotron losses contribute up most to 20 % reaching its maximum at the center of the magnetic arms. In the remaining regions, included the galactic center, ICS is dominating.

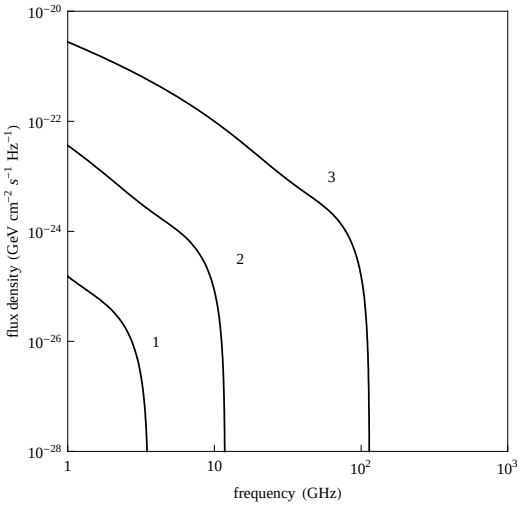

Figure 3.3: Synchrotron flux density from three different clumps. The neutralino parameters are $m_\chi c^2 = 100$ GeV and $\langle \sigma_{\rm A} v \rangle = 3 \times 10^{-26}$ cm^3 s^{-1}, while the relevant clumps parameters are shown in table 3.2.

reaches values as large as 50 eV/cm^3 in the inner kpc's. With this model the ICS is always the dominant energy loss process, also near the galactic center (see Fig.3.2). We thus have

$$\tau_{\rm ICS} = \tau^0_{\rm ICS} \left(\frac{U_{\rm rad}(\vec{r})}{\rm eV/cm^3} \right)^{-1} \left(\frac{E_e}{\rm GeV} \right)^{-1} , \tag{3.13}$$

with $\tau^0_{\rm ICS} = 9.82 \times 10^{15}$s.

Finally, considering both the energy losses $b_{\rm tot} = b_{\rm syn} + b_{\rm ICS}$ we have

$$\tau(E_e, \vec{r}) = \left(\frac{E_{\rm e}}{\rm GeV} \right)^{-1} \mu(\vec{r})\, \tau^0_{\rm syn} , \tag{3.14}$$

$$\mu(\vec{r}) = \left[\left(\frac{B(\vec{r})}{\mu \rm G} \right)^2 + \frac{\tau^0_{\rm syn}}{\tau^0_{\rm ICS}} \frac{U_{\rm rad}(\vec{r})}{\rm eV/cm^3} \right]^{-1} , \tag{3.15}$$

with the function $\mu(\vec{r})$ enclosing all the spatial dependence.

3.3 Synchrotron spectrum

The number of electrons and positrons with energy comprised between E_e and $E_e + {\rm d}E_e$, in the volume ${\rm d}V$ with position $\vec{r}$ is, by definition

$$\frac{{\rm d}n_e}{{\rm d}E_e}(E_e, \vec{r})\, {\rm d}E_e\, {\rm d}V \ . \tag{3.16}$$

During the time $\mathrm{d}t$ each $e^{\pm}$ loses, by synchrotron radiation, the amount of energy

$$\frac{\mathrm{d}E_{syn}}{\mathrm{d}t}\,\mathrm{d}t\ ,$$

cfr. eq. (1.4), therefore the total energy emitted by the $e^{\pm}$'s in the volume $\mathrm{d}V$ is

$$\mathrm{d}E_{emit} = \frac{\mathrm{d}n_e}{\mathrm{d}E_e}(E_e,\vec{r})\,\frac{\mathrm{d}E_{syn}}{\mathrm{d}t}\,\mathrm{d}E_e\,\mathrm{d}V\,\mathrm{d}t\ .$$

The synchrotron spectrum of an electron gyrating in a magnetic field has prominent peak at the resonance frequency

$$\nu = \frac{eB}{2\pi m_e}\left(\frac{E_e}{m_e c^2}\right)^2 = \nu_0\left(\frac{B}{\mu\mathrm{G}}\right)\left(\frac{E_e}{\mathrm{GeV}}\right)^2\ . \tag{3.17}$$

with $\nu_0 = 3.7\times 10^6\,\mathrm{Hz}$. This implies that, in practice, a δ–approximation around the peaks works extremely well. Using this *frequency peak* approximation the emitted energy can be related to its frequency:

$$E_e = m_e c^2\sqrt{\frac{2\pi m_e \nu}{eB}} = \left(\frac{\nu_0}{\mathrm{Hz}}\right)^{-1/2}\left(\frac{B}{\mu\mathrm{G}}\right)^{-1/2}\left(\frac{\nu}{\mathrm{Hz}}\right)^{1/2}\ \mathrm{GeV}\ .$$

This approximation permits us to define the *synchrotron emissivity* in the following simple way:

$$\begin{aligned} j_\nu(\nu,\vec{r}) &= \frac{\mathrm{d}E_{emit}}{\mathrm{d}V\,\mathrm{d}t\,\mathrm{d}\nu} \\ &= \frac{\mathrm{d}n_e}{\mathrm{d}E_e}(E_e(\nu),\vec{r})\,\frac{\mathrm{d}E_e}{\mathrm{d}\nu}\,\frac{\mathrm{d}E_{syn}}{\mathrm{d}t} \\ &= \frac{\pi}{3}\,\frac{c\sigma_T m_e B}{e\mu_0}\,\langle\sigma_{\mathrm{A}}v\rangle\,\tau(\vec{r})\left(\frac{\rho(\vec{r})}{m_\chi}\right)^2\left[F(1) - F\left(\frac{m_e}{m_\chi}\sqrt{\frac{2\pi m_e\nu}{eB}}\right)\right]. \end{aligned} \tag{3.18}$$

This quantity is then integrated along the line of sight for the various cases to get the final synchrotron flux across the sky.

3.3.1 Single clump signal

According to the description of chapter 1, let us consider a clump of mass m_{cl}, whose center of mass is placed at $\vec{R}_{\mathrm{cl}}$ and with a sufficiently small size.

In this case it is possible to neglect the spatial variation of $\mu(\vec{r})$ inside the clump itself, and thus the flux I_ν can be calculated as:

$$I_\nu(\nu, \vec{R}_{\rm cl}) = \frac{1}{4\pi\, d_{\rm cl}^2} \int {\rm d}\vec{r}'\, j_\nu(\nu, \vec{R}_{\rm cl} + \vec{r}') \ , \tag{3.19}$$

with $d_{\rm cl}$ the distance between the observer and the clump. Adopting the analytical approximation (3.5) I_ν can be rewritten as

$$I_\nu(\nu, \vec{R}_{\rm cl}) = I_\nu^0\, \mu(\vec{R}_{\rm cl}) \sum_k A_k \left(\frac{B(\vec{R}_{\rm cl})}{\mu{\rm G}}\right)^{1-\frac{k}{2}} \left(\frac{\nu}{\rm Hz}\right)^{\frac{k}{2}} \tag{3.20}$$

$$A_k(m_\chi) = b_k \left(\frac{m_\chi c^2}{\rm GeV}\right)^{-k} \left(\frac{\nu_0}{\rm Hz}\right)^{-\frac{k}{2}-1} , \tag{3.21}$$

with

$$\begin{aligned} I_\nu^0 \ &= \ 2.57\times 10^{-12} \left(\frac{m_\chi c^2}{100\,{\rm GeV}}\right)^{-3} \frac{\langle\sigma_{\rm A} v\rangle}{10^{-26}\,{\rm cm^3 s^{-1}}} \\ &\quad \times \left(\frac{r_{\rm cl}}{\rm kpc}\right)^3 \left(\frac{d_{\rm cl}}{\rm kpc}\right)^{-2} \left(\frac{\rho_{\rm cl}}{{\rm GeV}c^{-2}{\rm cm}^{-3}}\right)^2 {\rm GeV\ cm^{-2} s^{-1}\ Hz^{-1}} \ . \end{aligned} \tag{3.22}$$

Fig. 3.3 shows some examples of signal, produced by three clumps of our simulation. An important feature to notice is that the synchrotron signal sensibly depends on the magnetic field both for the normalization and for the covered frequency range. In particular, the signal frequency cutoff, remnant of the energy spectrum cutoff near m_χ, depends on B following the dependence in Eq. (3.17). Fig. 4.2 shows instead the positions and radio intensities for a realization of the clumps distribution with masses $m_{\rm cl} > 10^7 M_\odot$. It can be seen that all the clumps with a non negligible signal lies near the galactic plane where most of the galactic magnetic field is concentrated. Few clumps are visible at high latitude just for projection effects, being located very near and slightly up or below the solar position with respect to the galactic plane.

To have a reliable estimate of the sensitivity to a single clump detection diffusion effects cannot be neglected. Although the integrated synchrotron clump signal is given by Eq.(3.20), the clumps appears extended rather than pointlike with an extension typically of several degrees. As a reasonable approximation we can assume that the signal is spread over an area of radius equal to the diffusion length of the electrons $l_D = \sqrt{K(E_e)\tau_{\rm loss}(E_e)}$ where K is the diffusion coefficient and $\tau_{\rm loss}$ is the energy loss time given by Eq.

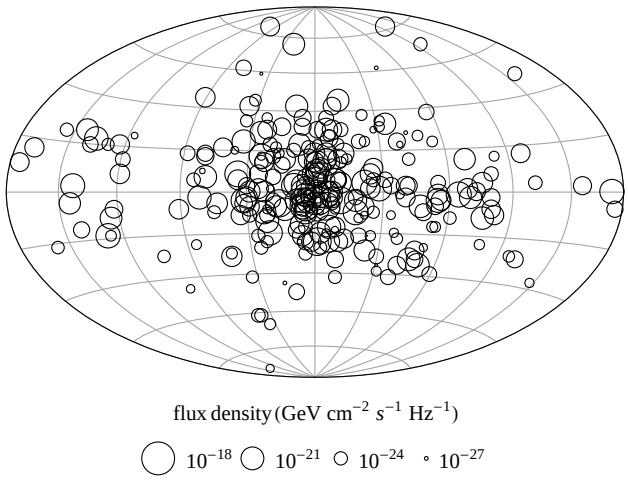

Figure 3.4: Sky map at the frequency of 1 GHz for a realization of clumps distribution. For each clump, the circle radius is proportional to the logarithm of radio flux.

(3.14). We use for K the Galprop model [101]

$$K = K_0 \left(\frac{E_e}{E_{e0}} \right)^{\delta} , \tag{3.23}$$

with a reference energy $E_{e0} = 3$ GeV, a Kolmogorov spectrum $\delta = 1/3$ and $K_0 = 10^{28}\mathrm{cm}^2/\mathrm{s}$.

Taking as reference the parameters of a very bright clump like the #3 in table 3.2, we get ($1\mathrm{pc} = 3 \times 10^{18}\mathrm{cm}$)

$$l_D = \sqrt{K(E_e) \left(\frac{E_\mathrm{e}}{\mathrm{GeV}} \right)^{-1} \mu(\vec{x})\, \tau^0_{\mathrm{syn}}} \approx 1\,\mathrm{kpc}\,, \tag{3.24}$$

for $E_e \approx 10$ GeV and for a radiation density $U_{\mathrm{rad}} \approx 5\,\mathrm{eV/cm}^3$. The energy losses are basically dominated by ICS thus the result is almost independent of the magnetic field value. Moreover the dependence from the electron energy and the radiation density itself is very weak. Of course the clumps will have a certain profile peaked in the center and will not be perfectly smoothed all over l_D. However the dilution of the signal in the much larger volume with respect to the region of emission makes quite hard to detect the clump. With a dilution over 1 kpc of a clump at a distance of 5 kpc with a flux of $10^{-22}\mathrm{GeV\,cm^{-2}s^{-1}Hz^{-1}}$ at 20 GHz, the clump emission is seen under a steradian $\pi\alpha^2 \approx 0.1$ sr with $\alpha \approx 10^\circ$, giving a diffuse clump flux of $10^{-21}\mathrm{GeV\,cm^{-2}s^{-1}Hz^{-1}sr^{-1}}$. The WMAP sensitivity of about 10μK

clump	$d_{\rm cl}$	$r_{\rm cl}$	$\rho_{\rm cl}$	B	flux density
#	kpc	kpc	$\mathrm{GeV}c^{-2}\mathrm{cm}^{-3}$	μG	$\mathrm{GeV\,cm^{-2}s^{-1}Hz^{-1}}$
1	14.2	0.180	6.51	0.0962	1.70×10^{-25}
2	4.71	0.181	6.50	0.320	4.55×10^{-23}
3	5.50	0.188	6.404	3.08	2.66×10^{-21}

Table 3.2: Parameters of the example clumps chosen in Fig. 3.3.

translates into a flux sensitivity [1] of $\sim 10^{-18}\mathrm{GeV\,cm^{-2}s^{-1}Hz^{-1}sr^{-1}}$, meaning that the expected, optimistic signal is about 3 order of magnitude below the reach of the current sensitivity. The situation is only slightly better at 150 MHz where the expected LOFAR sensitivity is 50 mK [106] i.e. $\sim 2 \times 10^{-19}\mathrm{GeV\,cm^{-2}s^{-1}Hz^{-1}sr^{-1}}$.

The chance of clump radio detection seems thus quite poor even with the next generation experiments. On the other side, the fact that the signal is anyway extended and not point-like makes the clump signal not really complementary to the diffuse component sharing the same systematics with a much fainter signal. It is likely thus that the a role for DM investigations in the radio will be played basically by the diffuse signal that we now calculate.

3.3.2 Diffuse signals

The diffuse halo signal is similarly given by the integral along the line of sight of Eq.(3.18)

$$\frac{\mathrm{d}^2 I_\nu}{\mathrm{d}l\,\mathrm{d}b} = \frac{\cos b}{4\pi} \int_0^\infty j_\nu \,\mathrm{d}s\,, \tag{3.25}$$

where (l, b) are coordinates on the sphere and the s the line of sight coordinate.

To calculate the total contribution from the substructures, instead, we have to sum over all haloes. The number of clumps inside the volume dV at distance R from the GC and mass comprised between m and $m + \mathrm{d}m$ is $\frac{\mathrm{d}n_{cl}}{\mathrm{d}m_{cl}}(m, R)\,\mathrm{d}m\,\mathrm{d}V$, eq. (1.9). Each one of these clumps gives rise to a flux I_ν given by (3.19). Therefore, what we have to do is integrate the quantity $\frac{\mathrm{d}n_{cl}}{\mathrm{d}m_{cl}}(m, R)\, I_\nu\,\mathrm{d}m\,\mathrm{d}V$ along the line of sight and over the desired mass range. In terms of the galactic coordinates the elementary volume $\mathrm{d}V$ is given by $\mathrm{d}V = s^2 \cos b\,\mathrm{d}s\,\mathrm{d}l\,\mathrm{d}b$, hence we obtain

$$\frac{\mathrm{d}^2 I_\nu^{\rm CL}}{\mathrm{d}l\,\mathrm{d}b} = \cos b \int_{m_1}^{m_2} \mathrm{d}m \int \mathrm{d}s\, s^2 \frac{\mathrm{d}n_{cl}}{\mathrm{d}m_{cl}}(m, R)\, I_\nu$$

[1] At radio frequencies the Rayleigh-Jeans law $F_\nu = 2\nu^2/c^2 k_B T$ is employed to translate fluxes into brightness temperatures

$$= \frac{A}{12}\left(\frac{1\,\mathrm{kpc}}{1\,\mathrm{cm}}\right)\left(\frac{m_\chi c^2}{\mathrm{GeV}}\right)^{-3}\left(\frac{\langle\sigma_\mathrm{A} v\rangle}{\mathrm{cm}^3\mathrm{s}^{-1}}\right)\frac{\cos b}{\mathrm{kpc}}\int \mathrm{d}s\left(\frac{R}{r_h}\right)^{-1}\left(1+\frac{R}{r_h}\right)^{-2}$$
$$\times\int_{m_1}^{m_2}\mathrm{d}m\left(\frac{m}{M_{cl}}\right)^{-2}{}^{2}\left(\frac{r_\mathrm{cl}}{\mathrm{kpc}}\right)^3 K(\mathbf{R},\nu)\ \mathrm{GeV\,cm^{-2}s^{-1}Hz^{-1}\ kpc^3}\ ,$$

where, for simplicity, we have defined

$$K(\mathbf{R},\nu)=\mu(\mathbf{R})\sum_k A_k\left(\frac{B}{\mu\mathrm{G}}\right)^{1-k/2}\left(\frac{\nu}{\mathrm{Hz}}\right)^{k/2}\ .$$

We can replace the integral over the mass with an integral over the concentration, $c = c_1\left(\frac{m}{M_\odot}\right)^{-\alpha}$ (see chapter 1). To this aim we rewrite all the quantities appearing in the integral in terms od c:

$$\left(\frac{r_\mathrm{cl}}{\mathrm{kpc}}\right)^3=\left(\frac{3M_\odot}{4\pi\Delta\rho_c}\mathrm{kpc}^{-3}\right)c_1^{\alpha^{-1}}c^{-(3+\alpha^{-1})}\ ,$$

$$\left(\frac{m}{M_{cl}}\right)^{-2}=\left(\frac{M_{cl}}{M_\odot}\right)^2 c_1^{-2\alpha^{-1}}c^{2\alpha^{-1}}\ ,$$

and

$$\left(\frac{\rho_\mathrm{cl}}{\mathrm{GeV}c^{-2}\mathrm{cm}^{-3}}\right)^2=\frac{\Delta^2}{9}\left(\frac{\rho_\mathrm{c}}{\mathrm{GeV}c^{-2}\mathrm{cm}^{-3}}\right)^2\frac{c^6}{\left[\log(1+c)-\frac{c}{1+c}\right]^2}$$

Hence

$$\int_{m_1}^{m_2}\mathrm{d}m\ldots = \frac{\Delta}{10\alpha\pi}\left(\frac{\mathrm{kpc}}{\mathrm{cm}}\right)^{-3}\left(\frac{\rho_\mathrm{c}}{\mathrm{GeV}c^{-2}\mathrm{cm}^{-3}}\right)\left(\frac{M_{cl}}{M_\odot}\right)^2\left(\frac{M_\odot}{\mathrm{GeV}c^{-2}}\right)^2$$
$$\times\int_{c(m_2)}^{c(m_1)}\frac{c^2\,\mathrm{d}c}{\left[\log(1+c)-\frac{c}{1+c}\right]^2}\,\mathrm{GeV}c^{-2}$$

Let us define $\Lambda(m_1,m_2)$ the dimensionless integral present in the last expression, and numerically calculate it for two example integration limits:

$$\Lambda(10^{-6}M_\odot,10^7M_\odot)=1.09\times10^4$$

and

$$\Lambda(10^{-6}M_\odot,10^{10}M_\odot)=1.13\times10^4\ .$$

This means that the difference in considering the signal produced by the entire clumps distribution or the one due to the low mass ones (from 10^{-6}

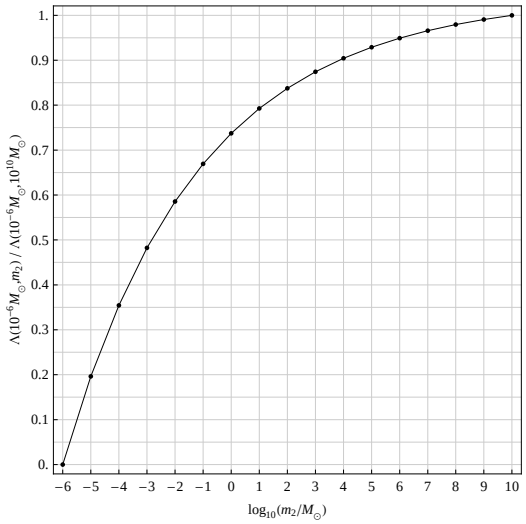

Figure 3.5: Ratio between the signal produced by the full substructures distribution and the one due to the clumps till a certain mass m_2 only.

to $10^7 M_\odot$) is about a negligible 3 %. This fact, jointly to the poor chance to resolve the single clumps, even the biggest ones, lead us to consider the whole clump distribution as a source of a second smooth signal to be added to the NFW one.

It results

$$\frac{\mathrm{d}^2 I_\nu^{\mathrm{CL}}}{\mathrm{d}l\,\mathrm{d}b} = I_0^{\mathrm{CL}} \frac{\cos b}{\mathrm{kpc}} \int \mathrm{d}s \left(\frac{R}{r_h}\right)^{-1} \left(1+\frac{R}{r_h}\right)^{-2} K(\mathbf{R},\nu)$$

with I_0^{CL} given by

$$\begin{aligned} I_0^{\mathrm{CL}} = {} & \frac{\Delta}{144}\,\frac{1}{4\pi^2 \ln 10}\left(\frac{1\,\mathrm{kpc}}{1\,\mathrm{cm}}\right)^{-2}\left(\frac{\rho_{\mathrm{c}}}{\mathrm{GeV}c^{-2}\mathrm{cm}^{-3}}\right)\frac{1}{\alpha}\left[\log(1+c_h)-\frac{c_h}{1+c_h}\right]^{-1} \\ & \times\left(\frac{M_\odot}{\mathrm{GeV}c^{-2}}\right)\times\left(\frac{M_{MW}}{M_\odot}\right)\frac{p_{1',2'}}{n_{2'}-n_{1'}}\left(\frac{r_{\mathrm{h}}}{\mathrm{kpc}}\right)^{-3}\Lambda(m_1,m_2) \\ & \times\left(\frac{m_\chi c^2}{\mathrm{GeV}}\right)^{-3}\left(\frac{\langle\sigma_{\mathrm{A}}v\rangle}{\mathrm{cm}^3\mathrm{s}^{-1}}\right)\mathrm{GeV\,cm^{-2}s^{-1}Hz^{-1}}\ . \end{aligned}$$

Substituting all constants but the neutralino parameters we obtain

$$I_0^{\mathrm{CL}} = 3.71\times10^{19}\left(\frac{m_\chi c^2}{\mathrm{GeV}}\right)^{-3}\left(\frac{\langle\sigma_{\mathrm{A}}v\rangle}{\mathrm{cm}^3\mathrm{s}^{-1}}\right)\ \mathrm{GeV\,cm^{-2}s^{-1}Hz^{-1}},$$

It is now an easy task to rewrite the integrated clumps signal in the same

form of the NFW case. It results

$$\frac{\mathrm{d}^2 I_\nu^{\mathrm{CL}}}{\mathrm{d}l\,\mathrm{d}b} = \frac{\cos b}{4\pi}\int j_\nu^{\mathrm{CL}}\mathrm{d}s$$

With a *total substructures emissivity* defined by

$$j_\nu^{\mathrm{CL}} = 0.151\left(\frac{R}{r_{\mathrm{h}}}\right)^{-1}\left(1+\frac{R}{r_{\mathrm{h}}}\right)^{-2} k(\mathbf{R},\nu)\mathrm{GeV\,cm^{-3}s^{-1}Hz^{-1}}\,.$$

Hence the sum of the two diffuse contributions can be rewritten as

$$\frac{\mathrm{d}^2 I_\nu^{\mathrm{DM}}}{\mathrm{d}l\,\mathrm{d}b} = \frac{\cos b}{4\pi}\int j_\nu^{\mathrm{DM}}\,\mathrm{d}s\,, \tag{3.26}$$

where[2]

$$\begin{aligned} j_\nu^{\mathrm{DM}} &= \frac{1}{4}\left(\frac{m_\chi c^2}{\mathrm{GeV}}\right)^{-3}\frac{\langle\sigma_{\mathrm{A}}v\rangle}{\mathrm{cm^3s^{-1}}}\left\{\left[\frac{\rho_{\mathrm{h}}/\mathrm{GeV}c^{-2}\mathrm{cm}^{-3}}{(r/r_{\mathrm{h}})(1+r/r_{\mathrm{h}})^2}\right]^2+\frac{\rho_{\mathrm{CL}}/\mathrm{GeV}c^{-2}\mathrm{cm}^{-3}}{(r/r_{\mathrm{h}})(1+r/r_{\mathrm{h}})^2}\right\} \\ &\quad\times\mu(\vec{r})\sum_k A_k(m_\chi)\left(\frac{B(\vec{r})}{\mu\mathrm{G}}\right)^{1-k/2}\left(\frac{\nu}{\mathrm{Hz}}\right)^{k/2}\mathrm{GeV\,cm^{-3}s^{-1}Hz^{-1}sr^{-1}}\,. \end{aligned} \tag{3.27}$$

Thus, from the point of view of DM annihilation the unresolved clumps signal behaves like a further smooth NFW component with the same scale radius of the halo profile, but with a different *effective density* $\rho_{\mathrm{CL}} = 0.604\,\mathrm{GeV}c^{-2}\mathrm{cm}^{-3}$, and with an emissivity simply proportional to the density profile instead of its square.

We see further that the halo component dominates in the central region of the galaxy, where

$$\frac{r}{r_{\mathrm{h}}}\left(1+\frac{r}{r_{\mathrm{h}}}\right)^2 < \frac{\rho_{\mathrm{h}}^2}{\rho_{\mathrm{CL}}} \quad\Rightarrow\quad r < 4.39\,\mathrm{kpc} \tag{3.28}$$

[2]Here, as in Eq. (3.18) the passage from the analytical approximation to the general case is made by the substitution

$$\sum_k A_k\left(\frac{B}{\mu\mathrm{G}}\right)^{1-k/2}\left(\frac{\nu}{\mathrm{Hz}}\right)^{k/2} =$$
$$\left(\frac{m_\chi c^2}{\mathrm{GeV}}\right)\left(\frac{\nu_0}{\mathrm{Hz}}\right)^{-1/2}\left(\frac{\nu}{\mathrm{Hz}}\right)^{-1/2}\left(\frac{B}{\mu\mathrm{G}}\right)^{3/2}\left[F(1)-F\left(\frac{m_e}{m_\chi}\sqrt{\frac{2\pi m_e\nu}{eB}}\right)\right]$$

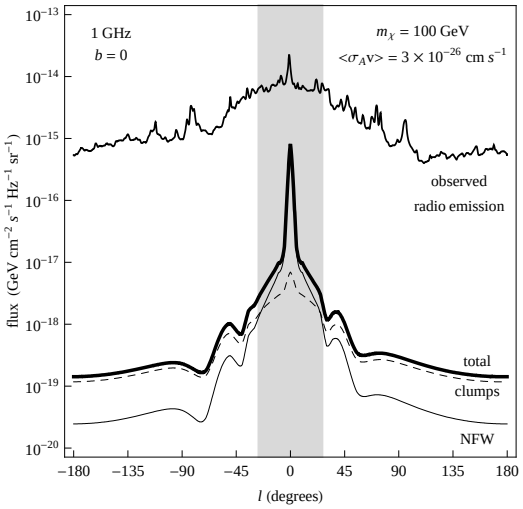

Figure 3.6: DM synchrotron profile for the Halo and unresolved substructures and their sum at 1 GHz for $m_\chi = 100$ GeV and $\langle \sigma_{\rm A} v \rangle = 3 \times 10^{-26}\,{\rm cm}^3{\rm s}^{-1}$. The astrophysical observed emission at the same frequency is also shown.

which corresponds to a disk of radius 27.3 degrees (see fig. 3.6).

Eq. (3.27) constitutes the main result of this chapter. The sky map obtained performing the integral (3.25) is showed in fig. 3.7. There a 100 GeV neutralino mass and an annihilation cross section such that $\langle \sigma_{\rm A} v \rangle = 3 \times 10^{-26}$ ${\rm cm}^3{\rm s}^{-1}$ are assumed.

Now that we know how to calculate the synchrotron emission due to dark matter annihilation we can proceed to the comparison of this with the observed galactic radio emission. This will be the main subject of the next chapter.

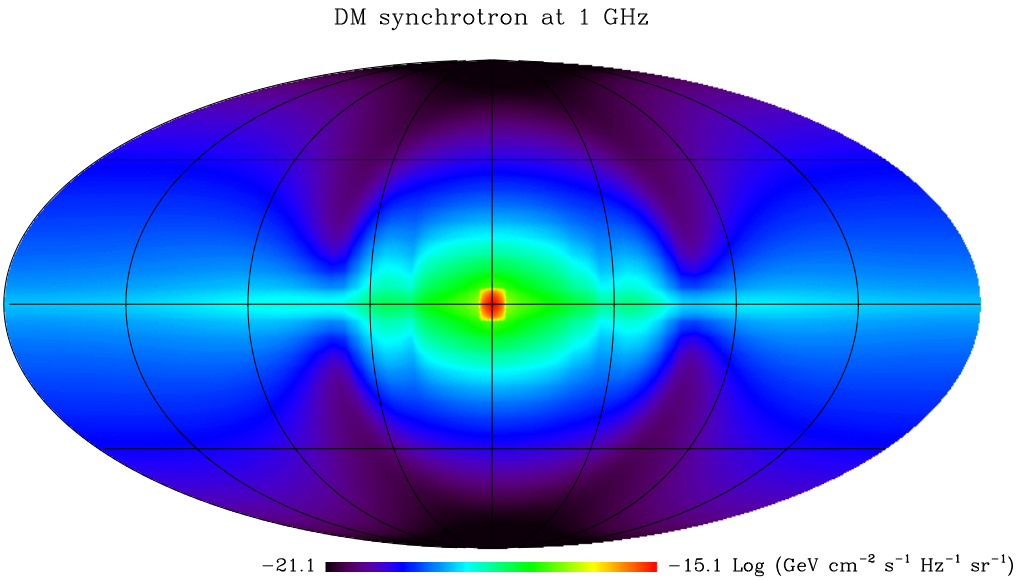

Figure 3.7: Sky map of the galactic radio signal generated by the DM smooth halo and unresolved clumps at the frequency of 1 GHz.

Chapter 4

Annihilation constraints from the radio sky

In this chapter we will derive constraints on the DM emission comparing the expected diffuse emission from the smooth halo and the unresolved population of clumps with all sky observation in the radio band.

4.1 Galactic radio foreground

In the frequency range between 100 MHz-100 GHz where the DM synchrotron signal is expected, various astrophysical processes contribute to the observed diffuse emission. Radio emission from galaxies is generally understood as arising from three effects. Competing synchrotron emission is given by Cosmic Ray electrons accelerated in supernovae shocks dominating the radio sky up to $\sim$ 10 GHz. At higher frequencies the Cosmic Microwave Background (CMB) and its anisotropies represents the main signal. However, thanks to the very sensitive multi-frequency survey by the WMAP satellite, this signal (which represents thus a background for DM searches) can be modeled in a detailed way and can thus be removed from the observed radio galactic emission [109]. The other two galactic processes contributing in the 10–100 GHz range are given by thermal bremsstrahlung (free-free emission) of electrons on the galactic ionized gas, and emission by small grains of vibrating dust.

Let us firstly examine the technique used to disentangle CMB anisotropies from the galactic radio foreground, then we will review each one of the foreground component in more detail.

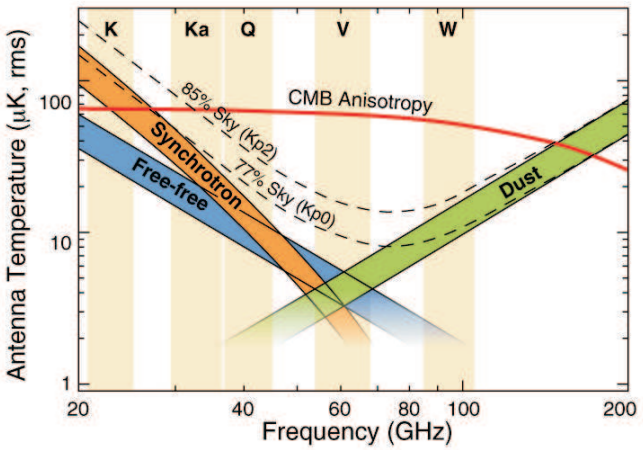

Figure 4.1: Relative contributes of the various galactic foregrounds.

4.1.1 CMB anisotropy subtraction

Galactic foreground signals can be distinguished from the anisotropy of the CMB due to their different spectra and their peculiar spatial distributions. To reliably separate Galactic foreground signals from CMB anisotropy a wide frequency coverage is needed. WMAP makes observations in five different frequency bands –named K, Ka, Q, V, and W– between 22 and 94 GHz:

Microwave Band	K	Ka	Q	V	W
Frequency (GHz)	22.8	30.0	40.7	60.8	93.5
Wavelength (mm)	13.6	10.0	7.5	5.0	3.3

The frequency dependence of the CMB anisotropy and of the three known galactic radio foreground are shown in figure 4.1.1 (in units of antenna temperature, see footnote on page 51). The vertical bars show the WMAP frequency bands.

The figure clearly shows that, far from galactic plane (the case represented in the figure), CMB anisotropy constitute the dominant emission in the frequency range 30-150 GHz, therefore to characterize galactic emissions the main information comes from observation in the two lowest frequency WMAP bands (K and Ka). This is done using two different techniques, fully described in [74] and briefly outlined here. Both techniques were successfully employed by COBE [75].

The first technique uses as foreground emission templates pre-existing information at low frequencies (radio and far-infrared). There are many uncertainties associated to this method. First of all, the uncertainties in the

original data are often big. The extrapolation of data at higher frequencies introduces errors due to the variations of the foreground spectral indices. Also, free-free emission never dominates the microwave foreground, therefore there is no good template for it.

The second technique consists in forming linear combinations of multi-frequency WMAP observations. This permits to cancel signals with specified spectra. This linear combination makes no assumptions about the foreground signal intensity or about its spatial distribution, nevertheless it requires assumptions on the foregrounds spectra.

WMAP uses five frequency bands to solve for the five possible signals, the four we already know, synchrotron, free-free, dust and CMB anisotropy, plus a possible fifth one. For example, there are hints of a foreground that might be due to rapidly spinning dust grains emitting microwave radiation [76], though the evidence for this is still quite tentative and so it is omitted in the showed plot. Also, if dark matter injects electron and positrons in our galaxy, the synchrotron signal we calculated in the previous chapter, surely constitutes a fifth component of the radio signal.

More important than the specific choice of frequencies is the range of frequency coverage. Till a maximum frequency of 22 GHz (atmospheric water line) ground based telescopes are able to make very accurate measurements, so 22 GHz marks the beginning of the frequency range of interest for an orbiting telescope like WMAP. The highest frequency should be order 100 GHz to explore the region where the dust contribution dominates over the CMB anisotropy (fig. 4.1.1). This permits to reduce the number of competing foreground signals. The choice of the particular frequencies between 22 and 100 GHz are determined by the more technical reasons.

4.1.2 Synchrotron emission

At lower radio frequencies the "non-thermal" synchrotron emission due to relativistic electrons spiraling in the GMF constitutes the dominant effect. Its flux decreases at higher frequencies approximately according to a power law ($\sim \nu^{-1}$).

More precisely, the energy distribution for high-energy electrons is not a pure power law, so neither is the spectrum for synchrotron radiation. In fact the highest energy electrons lose energy more quickly ($\tau_{syn} \propto E_e^{-1}$, eq. (3.12)) therefore their number is reduced in regions where they are not replenished. This energy loss determines a gradual steepening of the power law index by about 0.5 at frequencies above 10–100 MHz. Further, while the overall index (extrapolated from lower frequencies) is ≈ -0.7 [117, 118], higher frequencies may preferentially sample more energetic electron populations and thus have

a flatter index ($\beta \approx -0.5$) [119].

4.1.3 Free-free

The free–free emission is the "thermal" bremsstrahlung radiation from non-relativistic electron–ion interactions. Its flux that is nearly constant with frequency ($\sim \nu^{-0.1}$), therefore it becomes relatively more important than synchrotron at higher frequencies. At higher latitudes a typical crossover frequency is about 60 GHz, but can be 20 GHz or lower in specific regions in the Galactic plane. Free-free emission neither follow a strict power law, but its physics is well understood and the variation of the power–law index over the range 22–100 GHz is so small that –with respect to WMAP observations analysis– it can be simply neglected.

4.1.4 Dust

Is is well known that the interstellar medium contains many different types of molecules and dust grains with a broad range of physical properties. It was originally expected that in the far-infrared/submillimeter bands, all dust would have similar optical properties, with a predicted ν^2 emissivity [120].

Recent laboratory measurements suggest instead that universality of ν emissivity is quite an oversimplification. Different species of grains in fact posses differing emissivity laws. The abundance and composition of grains of different species can be constrained by astronomical observations. A multicomponent model for interstellar dust is due to Pollack and collaborators [121]. This model predicts that, due to the dominance of carbon species, at frequencies $\nu \gtrsim 500$ GHz, dust emission has to obey a $\nu^{2.6}$ emissivity law, while at lower frequencies, due to dominance of astronomical silicates emission, the emissivity flattens to a $\nu^{1.5}$ profile.

Vibrational dust emission is the dominant galactic foreground contribution above ∼60 GHz.

4.1.5 Spinning dust

In addition to these three foregrounds, much recent work has focused on the possibility of significant emission from rapidly rotating dust grains; this emission is thought to peak somewhere in the 10–30 GHz range and fall off roughly exponentially at higher frequencies.

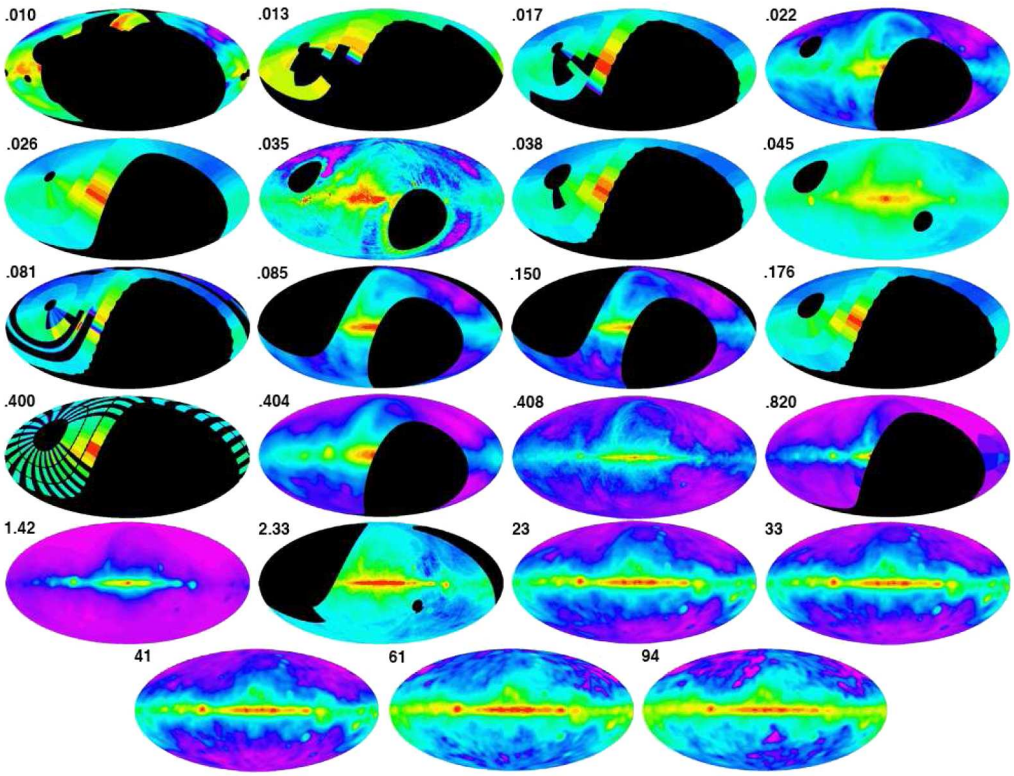

Figure 4.2: Library of radio maps from 0.010 GHz to 2.326 GHz and CMB-free WMAP foreground maps used in [110].

4.2 DM Annihilation constraints

In the following, our approach will be to compare the DM signal with the observed radio emission where only the CMB is modeled and removed. For this purpose we use the code described in [110] where most of the radio survey observations in the range 10 MHz-100 GHz (fig. 4.2) are collected and a scheme to derive interpolated, CMB cleaned sky maps at any frequency in this range is described.

A more model dependent approach would be of course to try to model and subtract also the remaining emissions (synchrotron, free-free, dust) so that to compare the expected DM signal with the residual radio map. This is indeed the approach followed in [111, 112] where residual maps at the 5 WMAP frequencies are derived using spatial templates for the various expected astrophysical components. The residual maps then exhibit the feature called the *WMAP haze*, which has been indeed interpreted as radio emission

related to DM annihilation [113, 20]. However, the fit procedure used for the Haze extraction matters and, for example, using more degrees of freedom to model the foregrounds as performed for example by the WMAP team [114] fails in finding the feature. We will anyway show for comparison the constraints derived using the Haze residual map at the WMAP frequency of 23 GHz [115] . We will see however that within our conservative approach comparable or better constraints with respect to use of the Haze map can be obtained thanks to the use of multi-frequency information. With a given DM mass, in fact, 23 GHz is generally not the best frequency to use and better constraints are instead obtained using observations at lower frequencies even without further foreground modeling.

Definitely, a detailed foreground modeling at all radio frequencies would clearly give much stronger constraints on the DM signal and/or eventually confirm the DM nature of the WMAP haze. To this purpose consistent progress will be achieved in the next years with the new high quality data coming from the PLANCK mission and from low frequency arrays like LOFAR and SKA.

The pattern and intensity of the DM radio map resulting from the sum of the contributions from the smooth halo and unresolved clumps is shown in Fig. 3.7 for $m_\chi = 100$ GeV and $\langle \sigma_{\rm A} v \rangle = 3 \times 10^{-26} {\rm cm}^3 {\rm s}^{-1}$. Similar maps are obtained at different frequencies and different m_χ and $\langle \sigma_{\rm A} v \rangle$ to obtain DM exclusion plots. For our analysis we use a small mask covering a $15^\circ \times 15^\circ$ region around the galactic center where other energy loss processes other than synchrotron and ICS start possibly to be relevant. We include the galactic plane although this region has basically no influence for the constraints on the DM signal.

In fig. 4.4 we show the radio constraints on the DM annihilation signal in the m_χ–$\langle \sigma_{\rm A} v \rangle$ plane for various frequencies and various choices of the background. Several comments are in order. First, we can see that, as expected, the use of the haze at 23 GHz gives about one order of magnitude better constraints with respect to the synchrotron foregrounds at the same frequency. However, using also the information at other frequencies almost the same constraints can be achieved. The information at other frequencies in particular is complementary giving better constraints at lower DM masses. This is easily understood since a smaller DM mass increases the annihilation signal ($\propto m_\chi^{-2}$) at smaller energies, and thus smaller synchrotron frequencies. In particular, the constraints improve of about one order of magnitude at $m_\chi \sim 100$ GeV from 23 GHz to 1 GHz while only a modest improvement is achieved considering further lower frequencies as 0.1 GHz. This saturation of the constraints is due to the frequency dependence of the DM signal that below 1 GHz becomes flatter than the astrophysical backgrounds so that the

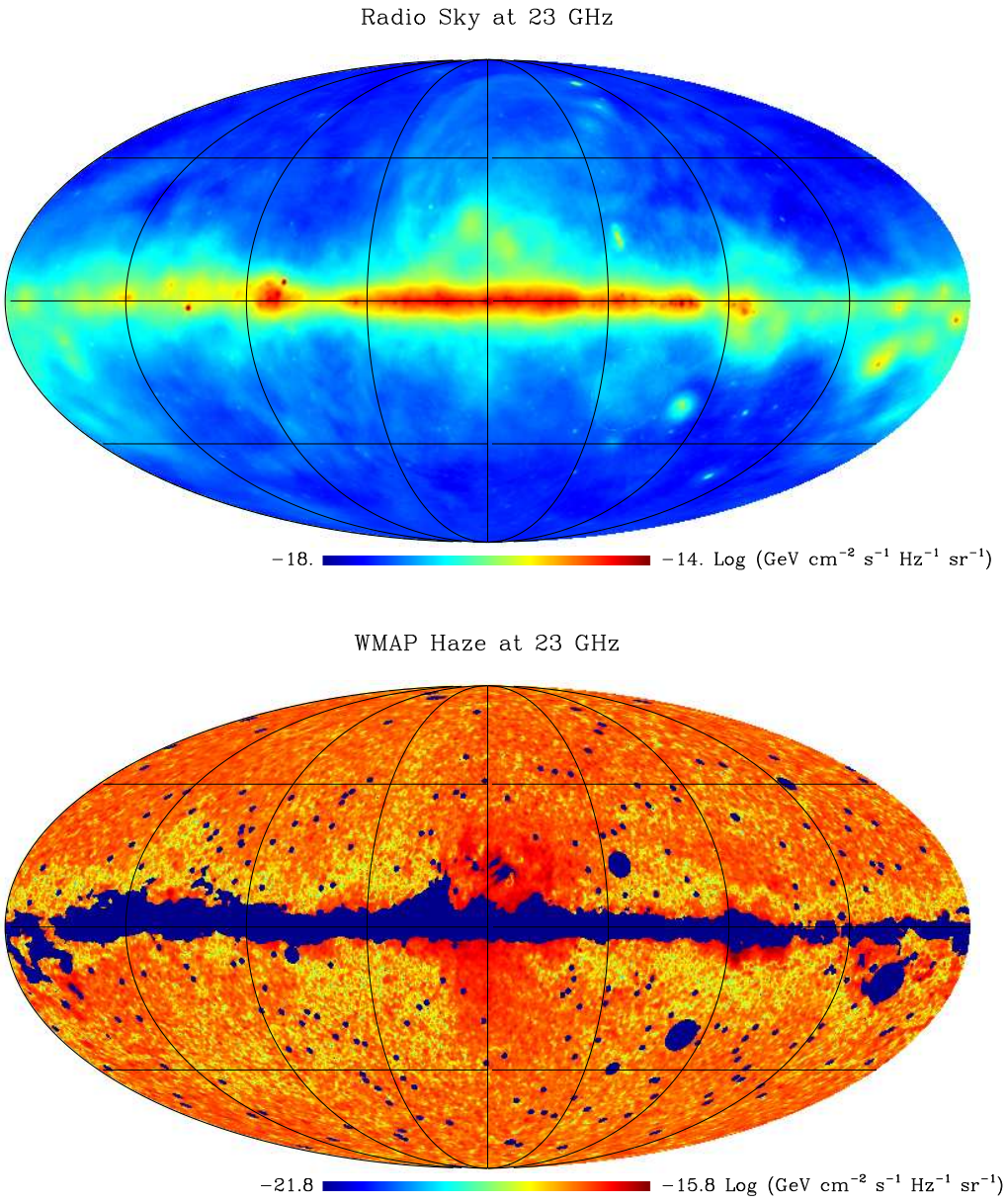

Figure 4.3: Sky map of galactic foregrounds at the frequency of 23 GHz (top), and of the residual map showing the WMAP Haze (bottom).

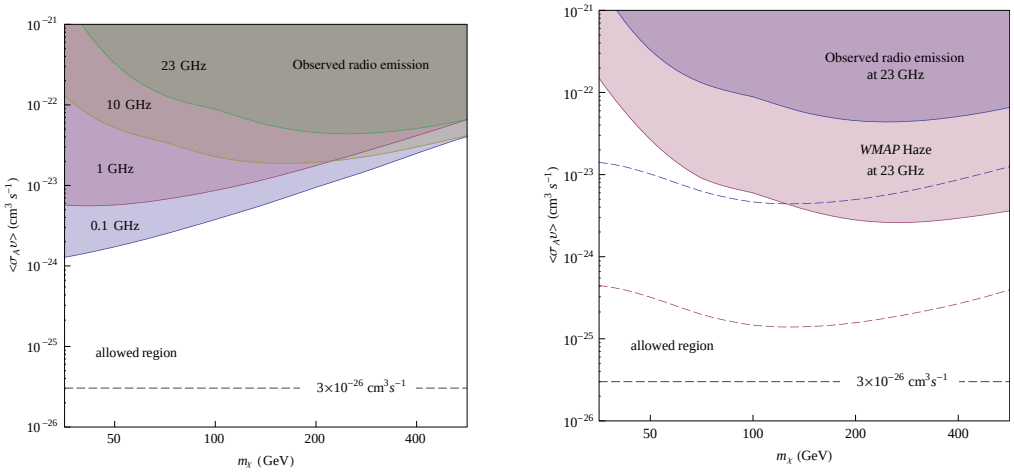

Figure 4.4: (Left) Constraints in the m_χ-$\langle\sigma_{\rm A} v\rangle$ plane for various frequencies without assuming synchrotron foreground removal. (Right) Constraints from the WMAP 23 GHz foreground map and 23 GHz foreground cleaned residual map (the WMAP Haze) for the TT model of magnetic field (filled regions) and for a uniform 10 μG field (dashed lines).

fraction of contribution from DM is maximal at about 1 GHz.

Notice that although the astrophysical background which we compare with at 1 GHz is an interpolation, the derived constraints are still valid given the smooth behavior and the broad frequency extent of the DM signal, which does not exhibit narrow peaks at particular frequencies. However, effective measurements have been performed for example at 408 MHz and 1.4 GHz (see [110]). Quoting our constraints at these exact frequencies would chance the results only slightly.

The DM signal has thus a broad frequency extent and also below 1 GHz is still relevant. This is a potential problem for the DM interpretation of the WMAP Haze given that, in the Haze extraction procedure, the observed radio emission at 408 MHz is used as template of the synchrotron background. In fact, naively, a DM signal at 23 GHz should be relevant at 408 MHz as well, unless either the DM mass or the magnetic field is quite high so that to shift the DM contribution to higher frequencies and making it negligible at 408 MHz.

The second relevant point to notice is that the constraint depends quite sensibly on the magnetic field assumptions. The constraints we obtain with the TT model are generally almost two order of magnitude weaker with respect to the results reported in [21]. They are instead more in agreement

with [22] where Galprop has been employed to calculate the DM synchrotron signal. For a closer comparison with [21] we choose, as they describe, a constant magnetic field of 10 μG although still keeping the Galprop ISRF model. Even in this case our derived constraints are a factor of 5 weaker (despite the inclusion of the contribution from substructures). The remaining factor of 5 can be finally recovered using a constant ISRF with $U_{\rm rad} = 5{\rm eV/cm}^3$ as assumed in [21] so that the smaller values of $U_{\rm rad}$ reduces the ICS losses enhancing in turn the synchrotron signal. It should be said however that, while the magnetic field normalization is still quite uncertain, the ISRF is instead more constrained and a large variation with respect to the Galprop model seems unlikely.

Summary and conclusions

Using conservative assumptions for the DM distribution in our galaxy we derive the expected secondary radiation due to synchrotron emission from high energy electrons produced in DM annihilation. The signal from single bright clumps offers only poor sensitivities because of diffusion effects which spread the electrons over large areas diluting the radio signal. The diffuse signal from the halo and the unresolved clumps is instead relevant and can be compared to the radio astrophysical background to derive constraints on the DM mass and annihilation cross section.

Constraints in the radio band, in particular, are complementary to similar (less stringent but less model dependent) constraints in the X-ray/gamma band [122, 123] and from neutrinos [124]. Radio data, in particular, are more sensitive in the GeV-TeV region while neutrinos provide more stringent bounds for very high DM masses ($\gtrsim 10$ TeV). Gammas, instead, are more constraining for $m_\chi \lesssim 1$ GeV. The combination of the various observations provides thus interesting constraints over a wide range of masses pushing the allowed window significantly near the thermal relic possibility.

More into details, we obtain conservative constraints at the level of $\langle \sigma_{\rm A} v \rangle \sim 10^{-23}\,{\rm cm}^3{\rm s}^{-1}$ for a DM mass $m_\chi = 100\,{\rm GeV}$ from the WMAP Haze at 23 GHz. However, depending on the astrophysical uncertainties, in particular on the assumption on the galactic magnetic field model, constraints as strong as $\langle \sigma_{\rm A} v \rangle \sim 10^{-25}\,{\rm cm}^3{\rm s}^{-1}$ can be achieved. Complementary to other works which employ the WMAP Haze at 23 GHz, we also use the information in a wide frequency band in the range 100 MHz-100 GHz. Adding this information the constraints become of the order of $\langle \sigma_{\rm A} v \rangle \sim 10^{-24}\,{\rm cm}^3{\rm s}^{-1}$ for a DM mass $m_\chi = 100\,{\rm GeV}$. The multi-frequency approach thus gives comparable constraints with respect to the WMAP Haze only, or generally better for $m_\chi \lesssim 100$ GeV where the best sensitivity is achieved at $\sim$ GHz frequencies.

The derived constraints are quite conservative because no attempt to model the astrophysical background is made differently from the case of the WMAP Haze. Indeed, the Haze residual map itself should be interpreted with some caution, given that the significance of the feature is at the mo-

ment still debated and complementary analyses from different groups (as the WMAP one) miss in finding a clear evidence of the feature. Definitely the multi-frequency approach will be necessary to test in a convincing way a possible DM signal like the claim related to the WMAP Haze. Progresses are expected with the forthcoming data at high frequencies from Planck and at low frequencies from LOFAR and, in a more distant future, from SKA. These surveys will help in disentangling the various astrophysical contributions thus assessing the real significance of the Haze feature. Further, the low frequency data in particular, will help to improve our knowledge of the galactic magnetic field. Progresses in these fields will provide a major improvement for the interpretation of the DM-radio connection.

Appendix A

Analytical approximation for the neutralino annihilation spectrum

What follows is the proof of result (3.5).

$$\begin{aligned}
\int_{E_\mu}^{E_\mu/\xi} \mathrm{d}E_\pi W_\pi(E_\pi) \frac{\mathrm{d}N_\mu^{(\pi)}}{\mathrm{d}E_\mu}(E_\pi) &= \frac{1}{m_\chi c^2}\,\frac{15}{16}\,\frac{1}{1-\xi}\int_{E_\mu/m_\chi c^2}^{(E_\mu/m_\chi c^2)/\xi} x^{-5/2}(1-x)^2\mathrm{d}x \\
&= \frac{1}{m_\chi c^2}\,\frac{15}{16}\,\frac{1}{1-\xi}\sum_{n=0}^{2} b_n \int_{E_\mu/m_\chi c^2}^{(E_\mu/m_\chi c^2)/\xi} x^{-\left(n+\frac{1}{2}\right)}\mathrm{d}x \\
&= \frac{1}{m_\chi c^2}\,\frac{15}{16}\,\frac{1}{1-\xi}\sum_{n=0}^{2} \frac{b_n}{\frac{1}{2}-n}\left[x^{\frac{1}{2}-n}\right]_{E_\mu/m_\chi c^2}^{(E_\mu/m_\chi c^2)/\xi} \\
&= \frac{1}{m_\chi c^2}\sum_{n=0}^{2} c_n \left(\frac{E_\mu}{m_\chi c^2}\right)^{\frac{1}{2}-n}
\end{aligned}$$

where $b_0 = 1$, $b_1 = -2$, $b_2 = 1$, and

$$c_n = \frac{15}{16}\,\frac{1}{1-\xi}\,\frac{b_n}{\frac{1}{2}-n}\left(\xi^{n-\frac{1}{2}}\right) .$$

Similarly the $dN_e^{(\mu)}/dE_e$ term can be write in this way:

$$\frac{\mathrm{d}N_e^{(\mu)}}{\mathrm{d}E_e}(E_e, E_\mu) = \frac{2}{m_\chi c^2}\sum_{m=0}^{3} d_m \left(\frac{E_e}{m_\chi c^2}\right)^m \left(\frac{E_\mu}{m_\chi c^2}\right)^{-(m+1)}$$

with

$$d_0 = \frac{5}{6} \ , \quad d_1 = 0 \ , \quad d_2 = -\frac{3}{2} \ , \quad d_3 = \frac{2}{3} \ .$$

So we can rewrite the spectrum as:

$$\begin{aligned}
\frac{\mathrm{d}N_e}{\mathrm{d}E_e} &= \frac{2}{m_\chi c^2} \sum_{n=0}^{2} \sum_{m=0}^{3} c_n d_m \left(\frac{E_e}{m_\chi c^2} \right)^m \int_{E_e/m_\chi c^2}^{1} x^{-(n+m+1/2)} dx \\
&= \frac{1}{m_\chi c^2} \sum_{n=0}^{2} \sum_{m=0}^{3} \frac{2 c_n d_m}{\frac{1}{2} - n - m} \left(\frac{E_e}{m_\chi c^2} \right)^m \left[1 - \left(\frac{E_e}{m_\chi c^2} \right)^{\frac{1}{2}-n-m} \right] \\
&= \frac{1}{m_\chi c^2} \sum_{j \in J} a_j \left(\frac{E_e}{m_\chi c^2} \right)^j
\end{aligned}$$

with $J = \{-\frac{3}{2}, -\frac{1}{2}, 0, \frac{1}{2}, 2, 3\}$ and

$$a_j = \sum_{n=0}^{2} \frac{2 c_n d_j}{\frac{1}{2} - n - j} \ , \qquad \text{if } j = -\frac{3}{2}, -\frac{1}{2}, \frac{1}{2}$$

or

$$a_j = -\sum_{m=0}^{3} \frac{2 c_{\frac{1}{2}-j} d_m}{j - m} \ , \qquad \text{if } j = 0, 2, 3 \ .$$

Using theese expressions it is possible to calculate the values reported in Table 3.1.

Bibliography

[1] E. Komatsu *et al.* [WMAP Collaboration], arXiv:0803.0547 [astro-ph].

[2] G. Bertone, D. Hooper and J. Silk, Phys. Rept. **405** (2005) 279 [arXiv:hep-ph/0404175].

[3] G. Jungman, M. Kamionkowski and K. Griest, Phys. Rept. **267** (1996) 195 [arXiv:hep-ph/9506380].

[4] L. Bergstrom, Rept. Prog. Phys. **63** (2000) 793 [arXiv:hep-ph/0002126].

[5] L. Bergstrom, J. Edsjo and P. Gondolo, Phys. Rev. D **58** (1998) 103519 [arXiv:hep-ph/9806293].

[6] V. D. Barger, F. Halzen, D. Hooper and C. Kao, Phys. Rev. D **65** (2002) 075022 [arXiv:hep-ph/0105182].

[7] E. A. Baltz and J. Edsjo, Phys. Rev. D **59** (1999) 023511 [arXiv:astro-ph/9808243].

[8] D. Hooper and J. Silk, Phys. Rev. D **71** (2005) 083503 [arXiv:hep-ph/0409104].

[9] F. Donato, N. Fornengo, D. Maurin and P. Salati, Phys. Rev. D **69** (2004) 063501 [arXiv:astro-ph/0306207].

[10] L. Bergstrom, M. Fairbairn and L. Pieri, Phys. Rev. D **74**, 123515 (2006) [arXiv:astro-ph/0607327].

[11] M. Regis and P. Ullio, Phys. Rev. D **78** (2008) 043505 [arXiv:0802.0234 [hep-ph]].

[12] T. E. Jeltema and S. Profumo, arXiv:0805.1054 [astro-ph].

[13] P. Blasi, A. V. Olinto and C. Tyler, Astropart. Phys. **18** (2003) 649 [arXiv:astro-ph/0202049].

[14] R. Aloisio, P. Blasi and A. V. Olinto, JCAP **0405** (2004) 007 [arXiv:astro-ph/0402588].

[15] A. Tasitsiomi, J. M. Siegal-Gaskins and A. V. Olinto, Astropart. Phys. **21** (2004) 637 [arXiv:astro-ph/0307375].

[16] L. Zhang and G. Sigl, arXiv:0807.3429 [astro-ph].

[17] S. Colafrancesco, S. Profumo and P. Ullio, Astron. Astrophys. **455** (2006) 21 [arXiv:astro-ph/0507575].

[18] S. Colafrancesco, S. Profumo and P. Ullio, Phys. Rev. D **75** (2007) 023513 [arXiv:astro-ph/0607073].

[19] E. A. Baltz and L. Wai, Phys. Rev. D **70** (2004) 023512 [arXiv:astro-ph/0403528].

[20] D. Hooper, D. P. Finkbeiner and G. Dobler, Phys. Rev. D **76** (2007) 083012 [arXiv:0705.3655 [astro-ph]].

[21] D. Hooper, Phys. Rev. D **77** (2008) 123523 [arXiv:0801.4378 [hep-ph]].

[22] P. Grajek, G. Kane, D. J. Phalen, A. Pierce and S. Watson, arXiv:0807.1508 [hep-ph].

[23] Zwicky, F. 1933, Helvetica Phys. Acta, **6**, 110.

[24] Smith, S. 1936, ApJ, **83**, 23.

[25] Kahn, F.D., & Woltjer, L. 1959, ApJ, **130**, 705.

[26] V.C. Rubin and K. Ford, Astrophys. J. 159 (1970) 379.

[27] K. G. Begeman, A. H. Broelis, and R. H. Sanders, Mon. Not. R. Astron. Soc. **249** (1991) 523.

[28] E. Holmberg, *Astrophys. J.* **94** (1941) 385.

[29] J. F. Navarro, C. S. Frenk and S. D. M. White, Astrophys. J. **490** (1997) 493 [arXiv:astro-ph/9611107].

[30] J. Diemand, B. Moore and J. Stadel, Nature **433** (2005) 389 [arXiv:astro-ph/0501589].

[31] J. Diemand, M. Kuhlen and P. Madau, Astrophys. J. **657** (2007) 262 [arXiv:astro-ph/0611370].

[32] M. Kuhlen, J. Diemand and P. Madau, arXiv:0805.4416 [astro-ph].

[33] V. Springel *et al.*, arXiv:0809.0898 [astro-ph].

[34] B. Moore, S. Ghigna, F. Governato, G. Lake, T. R. Quinn, J. Stadel and P. Tozzi, Astrophys. J. **524** (1999) L19.

[35] J.N. Bahcall, M. Schmidt, R.M. Soneira, Astrophys. J. 265 (1983) 730.

[36] R.R. Caldwell, J.P. Ostriker, Astrophys. J. 251 (1981) 61.

[37] M.S. Turner, Phys. Rev. D 33 (1986) 889.

[38] A.V. Kravtsov, A.A. Klypin, J.S. Bullock, J.R. Primack, Astrophys. J. 502 (1998) 48 [arXiv:astro-ph/9708176].

[39] L. Bergstrom, P. Ullio, J.H. Buckley, Astropart. Phys. 9 (1998) 137 [arXiv:astro-ph/9712318].

[40] S. Hofmann, D. J. Schwarz and H. Stoecker, Phys. Rev. D **64** (2001) 083507 [arXiv:astro-ph/0104173].

[41] A. M. Green, S. Hofmann and D. J. Schwarz, JCAP **0508** (2005) 003 [arXiv:astro-ph/0503387].

[42] J. S. Bullock *et al.*, Mon. Not. Roy. Astron. Soc. **321** (2001) 559 [arXiv:astro-ph/9908159].

[43] L. Pieri, G. Bertone and E. Branchini, Mon. Not. Roy. Astron. Soc. **384** (2008) 1627 [arXiv:0706.2101 [astro-ph]].

[44] Hiltner W.A., 1949, Astrophys. J. 109, 471

[45] Rand R.J., Kulkarni S.R., 1989, 343, 760

[46] Beck R., 2001, Space Science Reviews 99 (1), 243

[47] Widrow L.M., Preprint astro-ph/0207240 v1, accepted for publication in Reviews of Modern Physics

[48] Han J.L., 2002, AIP Conference Proceedings 609, 96

[49] J. Han, in "Astrophysical Polarized Backgrounds", American Institute of Physics, edited by S. Cecchini *et al.*, p. 96 (2002) [astro-ph/0110319].

[50] R. Beck, in "The Astrophysics of Galactic Cosmic Rays", eds. R. Diehl *et al.*, Space Science Reviews, Kluwer [astro-ph/0012402].

[51] T. Stanev, Astrophys. J. **479**, 290 (1997).

[52] P. G. Tinyakov and I. I. Tkachev, Astropart. Phys. **18**, 165 (2002) [astro-ph/0111305].

[53] R. J. Rand and A. G. Lyne, Mon. Not. Roy. Astron. Soc. **268**, 497 (1994).

[54] K. Beuermann, G. Kanbach, E. M. Berkhuijsen, Astron. Astrophys. **153**, 17 (1985).

[55] J. L. Han, R. N. Manchester, E. M. Berkhuijsen, R. Beck, Astron. Astrophys. **322**, 98 (1997).

[56] J. L. Han, R. N. Manchester, G. J. Qiao, Mon. Not. Roy. Astron. Soc. **306**, 371 (1999).

[57] J. L. Han and G. J. Qiao, Astron. Astrophys. **288**, 759 (1994).

[58] J. L. Han, R. N. Manchester, G. J. Qiao and A. G. Lyne, in "Radio Pulsars", APS Conf. Ser., editted by M. Bailes *et al.* [astro-ph/0211197].

[59] X. H. Sun, W. Reich, A. Waelkens and T. Ensslin, Astron. Astrophys. **477** (2008) 573-592 arXiv:0711.1572 [astro-ph].

[60] A. Noutsos, S. Johnston, M. Kramer and A. Karastergiou, Mon. Not. Roy. Astron. Soc. **386** (2008), 1881-1896 arXiv:0803.0677 [astro-ph].

[61] T.A. Porter and A.W. Strong, 29th International Cosmic Rays Conference Pune (2005), **00**, 101.

[62] Wainscoat, R. J., et al., ApJS 83, 111 (1992).

[63] Strong, A. W., Moskalenko, I. V. & Reimer, O., ApJ 537, 763 (2000).

[64] Kylafis, N. D. & Bahcall, J. N., ApJ 317, 637 (1987).

[65] Serpico et al., JCAP 0412 (2004) 010; astro-ph/0408076. et al.

[66] M. Milgrom, Astrophys. J. **270** (1983) 365.

[67] E.W. Kolb, M.S. Turner, The Early Universe, Addison-Wesley, Redwood City (Ca) 1990.

[68] K. Griest and M. Kamionkowski, Phys. Rev. Lett. **64** (1990) 615.

[69] Griest, K., & Seckel, D. 1991, Phys. Rev. D, 43, 3191

[70] G.F. Giudice, I. Tkachev and A. Riotto, Journal of High Energy Physics **9908** (1999) 009.

[71] D.J.H. Chung, E.W. Kolb and A. Riotto, Phys. Rev. **D60** (1999) 063504.

[72] J. Ellis, J. Lopez and D.V. Nanopoulos, Phys. Lett. **B247** (1990) 257; J. Ellis et al., Nucl. Phys. **B373** (1992) 399.

[73] P. Binetruy, Lecture course notes: "Supersymmetry: from concepts to searches".

[74] Gold et al. 2008, arXiv:0803.0715v1

[75] Kogut et al., ApJ, 470, (1996) 653.

[76] D. P. Finkbeiner et al.,arXiv:astro-ph/0408292

[77] P. D. Collins, A. D. Martin and E. J. Squires, "Particle Physics And Cosmology," New York, USA, Wiley (1989).

[78] J. Wess and J. Bagger, "Supersymmetry And Supergravity", Princeton, USA: Univ. Pr. (1992).

[79] A. Djouadi *et al.* [MSSM Working Group Collaboration], *Talk at Groupement de Recherche-Supersymetrie, Montpellier, France*, (1998) [arXiv:hep-ph/9901246].

[80] S. P. Martin, arXiv:hep-ph/9709356.

[81] K. A. Olive, TASI lectures on dark matter, arXiv:astro-ph/0301505.

[82] D. J. H. Chung, L. L. Everett, G. L. Kane, S. F. King, J. Lykken and L. T. Wang, arXiv:hep-ph/0312378.

[83] U. Amaldi, W. de Boer and H. Furstenau, Phys. Lett. B **260**, 447 (1991).

[84] Coleman e Mandula, Phys. Rev. 159 (1967) 1251.

[85] R. Haag, J. T. Lopuszanski and M. Sohnius, Nucl. Phys. B **88**, 257 (1975).

[86] N. Fornengo, Materia oscura: abbondanza fossile e possibili segnali di rivelazione, PhD Thesis, Torino, 1994.

[87] L. Roszkowski, Phys. Rev. **D50** (1994) 4842.

[88] P. Hut, Phys. Lett. **69B** (1977) 85.

[89] B.W. Lee and S. Weinberg, Phys. Rev. Lett. **39** (1977) 165.

[90] M.I. Vysotsky, A.D. Dolgov and Ya. B. Zel'dovich, JETP Lett. **26** (1977) 188.

[91] J. E. Gunn, B.W. Lee, I. Lerche, D.N. Schramm and G. Steigman, Astrophys. J. **223** (1978) 1015.

[92] P. Fayet, Phys. Lett. **86B** (1979) 272.

[93] N. Cabibbo, G. Farrar and L. Maiani, Phys. Lett. **105B** (1981) 155.

[94] H. Pagels and J.R. Primack, Phys. Rev. Lett. **48** (1982) 223.

[95] S. Weinberg, Phys. Rev. Lett. **50** (1983) 387.

[96] H. Goldberg, Phys. Rev. Lett. **50** (1983) 1419.

[97] L.M. Krauss, Nucl. Phys. **B227** (1983) 556.

[98] J. Ellis, J.S. Hagelin, D.V. Nanopoulos, K. Olive, M. Srednicki, Nucl. Phys. **B238** (1984) 453.

[99] J. Edsjo, Ph. D Thesis, arXiv:hep-ph/9704384.

[100] J. Ellis, S. Kelley and D.V. Nanopoulos, Phys. Lett., **260** (1991) 131

[101] I. V. Moskalenko and A. W. Strong, Astrophys. J. **493** (1998) 694 [arXiv:astro-ph/9710124].

[102] A. W. Strong and I. V. Moskalenko, Astrophys. J. **509** (1998) 212 [arXiv:astro-ph/9807150].

[103] A. W. Strong, I. V. Moskalenko and O. Reimer, Astrophys. J. **537** (2000) 763 [Erratum-ibid. **541** (2000) 1109] [arXiv:astro-ph/9811296].

[104] M.S. Longair, *High Energy Astrophysics* (2nd ed.), Cambridge University Press, Cambridge, 1982.

[105] T. A. Porter and A. W. Strong, arXiv:astro-ph/0507119.

[106] V. Jelic *et al.*, arXiv:0804.1130 [astro-ph].

[107] M. Prouza and R. Smida, Astron. Astrophys. **410** (2003) 1 [arXiv:astro-ph/0307165].

[108] M. Kachelriess, P. D. Serpico and M. Teshima, Astropart. Phys. **26** (2006) 378 [arXiv:astro-ph/0510444].

[109] M. Tegmark, A. de Oliveira-Costa and A. Hamilton, Phys. Rev. D **68** (2003) 123523 [arXiv:astro-ph/0302496].

[110] A. de Oliveira-Costa, M. Tegmark, B. M. Gaensler, J. Jonas, T. L. Landecker and P. Reich, arXiv:0802.1525 [astro-ph].

[111] D. P. Finkbeiner, Astrophys. J. **614** (2004) 186 [arXiv:astro-ph/0311547].

[112] G. Dobler and D. P. Finkbeiner, arXiv:0712.1038 [astro-ph].

[113] D. P. Finkbeiner, arXiv:astro-ph/0409027.

[114] B. Gold *et al.* [WMAP Collaboration], arXiv:0803.0715 [astro-ph].

[115] http://www.skymaps.info/

[116] Bold et al. arXiv:0803.0715 [astro-ph].

[117] Reich et al. 2004, in "The Magnetized Interstellar Medium" (Eds. B. Uyanyker, W. Reich, R. Wielebinski; Copernicus GmbH)

[118] Lawson et al., 1987, MNRAS, 225, 307.

[119] C. L. Bennett et al. 2003, ApJS, 148, 97

[120] Draine, B. T., & Lee, H. M. 1984, ApJ, 285, 89

[121] Pollack et al., Astrophys. J. 421, (1994) 615

[122] G. D. Mack, T. D. Jacques, J. F. Beacom, N. F. Bell and H. Yuksel, arXiv:0803.0157 [astro-ph].

[123] M. Kachelriess and P. D. Serpico, Phys. Rev. D **76** (2007) 063516 [arXiv:0707.0209 [hep-ph]].

[124] H. Yuksel, S. Horiuchi, J. F. Beacom and S. Ando, Phys. Rev. D **76** (2007) 123506 [arXiv:0707.0196 [astro-ph]].